

Chulalongkorn University

## Chula Digital Collections

---

Chulalongkorn University Theses and Dissertations (Chula ETD)

---

2018

### Investigation of Parameters for Metallic Artifact Reduction using 3-D SPACE in MR Lumbar Spine at 1.5 Tesla: A Phantom Study

Thanatchaya Lowong  
*Faculty of Medicine*

Follow this and additional works at: <https://digital.car.chula.ac.th/chulaetd>



Part of the [Radiation Medicine Commons](#)

---

#### Recommended Citation

Lowong, Thanatchaya, "Investigation of Parameters for Metallic Artifact Reduction using 3-D SPACE in MR Lumbar Spine at 1.5 Tesla: A Phantom Study" (2018). *Chulalongkorn University Theses and Dissertations (Chula ETD)*. 2475.

<https://digital.car.chula.ac.th/chulaetd/2475>

This Thesis is brought to you for free and open access by Chula Digital Collections. It has been accepted for inclusion in Chulalongkorn University Theses and Dissertations (Chula ETD) by an authorized administrator of Chula Digital Collections. For more information, please contact [ChulaDC@car.chula.ac.th](mailto:ChulaDC@car.chula.ac.th).

Investigation of Parameters for Metallic Artifact Reduction  
using 3-D SPACE in MR Lumbar Spine at 1.5 Tesla: A  
Phantom Study

Miss Thanatchaya Lowong



A Thesis Submitted in Partial Fulfillment of the Requirements  
for the Degree of Master of Science in Medical Imaging  
Department of Radiology  
Faculty of Medicine  
Chulalongkorn University  
Academic Year 2018  
Copyright of Chulalongkorn University

การหาพารามิเตอร์เพื่อลดสัญญาณแปลกปลอมที่เกิดจากโลหะโดยใช้เทคนิคสเปซแบบสามมิติใน  
การตรวจกระดูกสันหลังส่วนเอวด้วยเครื่องเอ็มอาร์ไอ 1.5 เทสลา: การศึกษาในหุ่นจำลอง



น.ส.ชนัญญา หล่อวงศ์

วิทยานิพนธ์นี้เป็นส่วนหนึ่งของการศึกษาตามหลักสูตรปริญญาวิทยาศาสตรมหาบัณฑิต  
สาขาวิชาสาขาเวชศาสตร์ ภาควิชารังสีวิทยา  
คณะแพทยศาสตร์ จุฬาลงกรณ์มหาวิทยาลัย  
ปีการศึกษา 2561  
ลิขสิทธิ์ของจุฬาลงกรณ์มหาวิทยาลัย

Thesis Title	Investigation of Parameters for Metallic Artifact Reduction using 3-D SPACE in MR Lumbar Spine at 1.5 Tesla: A Phantom Study
By	Miss Thanatchaya Lowong
Field of Study	Medical Imaging
Thesis Advisor	Assistant Professor KITIWAT KHAMWAN, Ph.D.

---

Accepted by the Faculty of Medicine, Chulalongkorn University in Partial  
Fulfillment of the Requirement for the Master of Science

Dean of the Faculty of Medicine

.....  
(Professor SUTTIPONG WACHARASINDHU, M.D.)

#### THESIS COMMITTEE

Chairman

.....  
(Associate Professor ANCHALI KRISANACHINDA,  
Ph.D.)

Thesis Advisor

.....  
(Assistant Professor KITIWAT KHAMWAN, Ph.D.)

Examiner

.....  
(Associate Professor Kosuke Matsubara, Ph.D.)

External Examiner

.....  
(Professor Franco Milano)

จุฬาลงกรณ์มหาวิทยาลัย  
CHULALONGKORN UNIVERSITY

รณัญญา หล่องค์ : การหาพารามิเตอร์เพื่อลดสัญญาณแปลกปลอมที่เกิดจากโลหะ โดยใช้เทคนิคสเปซแบบสามมิติในการตรวจกระดูกสันหลังส่วนเอว ด้วยเครื่องเอ็มอาร์ไอ 1.5 เทสลา: การศึกษาในหุ่นจำลอง. ( Investigation of Parameters for Metallic Artifact Reduction using 3-D SPACE in MR Lumbar Spine at 1.5 Tesla: A Phantom Study) อ.ที่ปรึกษาหลัก : ศศ. ดร.กิติวัฒน์ คำวัน

ผู้ป่วยที่ได้รับการผ่าตัดใส่เหล็กที่กระดูกสันหลังจะมีข้อจำกัดในการตรวจด้วยเครื่องเอกซเรย์ทอมografiแบบแม่เหล็กไฟฟ้าเนื่องจากโลหะจะเหนี่ยวนำให้สนามแม่เหล็กไม่เสถียร ทำให้เกิดสัญญาณแปลกปลอมบนภาพ วิทยานิพนธ์ฉบับนี้มีวัตถุประสงค์เพื่อหาค่าพารามิเตอร์สำหรับการลดสัญญาณแปลกปลอมที่เกิดจากโลหะในการตรวจกระดูกสันหลังส่วนเอวด้วยเครื่องเอ็มอาร์ไอ 1.5 เทสลา โดยการเก็บภาพด้วยเทคนิคสเปซแบบสามมิติ ซึ่งเป็นเทคนิคการสแกนขั้นสูงแบบใหม่ที่ได้รับให้เหมาะสมกับความคมชัดโดยใช้การพลิกมุมของโปรตอนที่แตกต่างกัน หรือเรียกว่า **Sampling Perfection with Application Optimized Contrasts using Different Flip Angle Evolutions (SPACE)** ทำการเก็บข้อมูลโดยนำหุ่นจำลองทรงกระบอกบรรจุน้ำที่มีส่วนผสมของนิกเกิลคลอไรด์ไฮดรต 3.3 กรัม/ลิตร และโซเดียมคลอไรด์ 2.4 กรัม/ลิตร โดยใช้โลหะ 2 ชนิด ได้แก่ สเตนเลสสตีลและไทเทเนียมบรรจุลงในหุ่นจำลอง แล้วนำไปสแกนด้วยเครื่องเอ็มอาร์ไอ 1.5 เทสลา โดยใช้เทคนิคเทอร์โบสปินเอคโค่ (Turbo spin echo) และสเปซแบบสามมิติในภาพ T2- weighted โดยทำการปรับค่าพารามิเตอร์ของช่องตัวรับสัญญาณ 3 ค่า ได้แก่ 296, 501, 723 เอิร์ตซ์/พิกเซล และค่าพลิกมุมที่  $100^\circ, 150^\circ, 180^\circ$  เพื่อหาค่าพารามิเตอร์ที่เหมาะสมสำหรับเทคนิคสเปซ นำภาพที่ได้จากการสแกนหุ่นจำลองไปคำนวณหาช่วงของความเข้มสัญญาณด้วยการใช้อัลกอริทึมเพื่อหาค่าเฉลี่ยความเข้มสัญญาณและส่วนเบี่ยงเบนมาตรฐาน และนำค่าที่ได้ไปใช้กับภาพที่ได้จากการสแกนหุ่นเพื่อคำนวณหาปริมาณของความเข้มสัญญาณแปลกปลอมจากโลหะโดยเทคนิคการกำหนดค่าระดับกัน (Thresholding technique) ค่าสัญญาณที่อยู่นอกช่วงปกติของความเข้มสัญญาณจะถูกคำนวณว่าเป็นสัญญาณแปลกปลอมจากโลหะ ทำการประเมินคุณภาพของภาพแต่ละโปรโตคอลด้วยการหาค่าเอสเอ็นอาร์ โปรโตคอลที่เหมาะสมจะถูกกำหนดโดยการเรียงลำดับคะแนนในเชิงของขนาดของสัญญาณแปลกปลอมจากโลหะ, ค่าเอสเอ็นอาร์ และค่าดูกลืนพลังงานจำเพาะ

ผลการศึกษาในหุ่นจำลองด้วยการใช้เทคนิคสเปซแบบสามมิติ (โปรโตคอล 1-9) และเทคนิคเทอร์โบสปินเอคโค่ (โปรโตคอล 10) พบว่าค่าเฉลี่ยขนาดสัญญาณแปลกปลอมจากโลหะชนิดสเตนเลสสตีลของโปรโตคอล 1-10 มีค่าเท่ากับ  $162.64 \pm 1.88, 158.30 \pm 1.79, 157.82 \pm 2.36, 126.43 \pm 1.22, 124.87 \pm 0.29, 122.93 \pm 1.57, 117.55 \pm 1.03, 114.82 \pm 1.55, 112.40 \pm 0.43$  และ  $184.89 \pm 1.19$  ลูกบาศก์เซนติเมตร และค่าเฉลี่ยขนาดสัญญาณแปลกปลอมจากโลหะชนิดไทเทเนียมของโปรโตคอล 1-10 มีค่าเท่ากับ  $33.80 \pm 1.03, 32.56 \pm 0.48, 33.79 \pm 0.90, 13.39 \pm 0.67, 13.77 \pm 0.73, 12.74 \pm 0.48, 10.89 \pm 0.77, 11.42 \pm 0.64, 10.67 \pm 0.71$  และ  $38.86 \pm 0.97$  ลูกบาศก์เซนติเมตร ตามลำดับ โปรโตคอลที่สามารถลดสัญญาณแปลกปลอมจากโลหะได้มากที่สุดคือ โปรโตคอล 9 ประมาณ 39.21% สำหรับสเตนเลสสตีล และ 72.55% สำหรับไทเทเนียม

จากผลการศึกษา สรุปได้ว่าเทคนิคสเปซสามารถลดสัญญาณแปลกปลอมจากโลหะได้อย่างมีประสิทธิภาพด้วยการเพิ่มช่องตัวรับสัญญาณมากขึ้น โดยโปรโตคอลที่เหมาะสมสำหรับการลดสัญญาณแปลกปลอมที่เกิดจากโลหะโดยการเก็บภาพด้วยเทคนิคสเปซแบบสามมิติในงานวิจัยนี้คือ การใช้ช่องตัวรับสัญญาณที่ 501เอิร์ตซ์/พิกเซล ค่าพลิกมุม  $100^\circ$  และ  $150^\circ$  สำหรับโลหะทั้งสองชนิด

สาขาวิชา วิทยาศาสตร์  
ปีการศึกษา 2561

ลายมือชื่อนิติศ .....  
ลายมือชื่อ อ.ที่ปรึกษาหลัก .....

# # 6074061130 : MAJOR MEDICAL IMAGING

KEYWORD: magnetic resonance imaging, metallic artifact reduction, SPACE pulse sequence, specific absorption rate

Thanatchaya Lowong : Investigation of Parameters for Metallic Artifact Reduction using 3-D SPACE in MR Lumbar Spine at 1.5 Tesla: A Phantom Study. Advisor: Asst. Prof. KITIWAT KHAMWAN, Ph.D.

Metallic artifact reduction in magnetic resonance imaging (MRI) has increasingly interested especially metal implant postoperative in lumbar spine. Recently, the new pulse sequence based on true isotropic 3D voxel with high resolution namely Sampling Perfection with Application Optimized Contrasts using Different Flip Angle Evolutions (SPACE) was introduced. This study aimed to determine the appropriate 3D T2-SPACE parameters for reducing the metallic artifact in MR lumbar spine 1.5 Tesla. Cylindrical phantom filled with 3.3 g/L,  $\text{NiCl}_2 \cdot 6\text{H}_2\text{O}$  and 2.4 g/L NaCl solution, and two commonly used metal implants (stainless steel and titanium) for lumbar spine were acquired using turbo spin echo (TSE) and SPACE pulse sequences in T2-weighted image contrast. A receiver bandwidth of 296, 501, 723 Hz/pixel and flip angle at  $100^\circ$ ,  $150^\circ$ ,  $180^\circ$  were adjusted in order to determine the 3D T2-SPACE appropriate parameters. The volume of metal artifact was quantitatively assessed by applying a histogram distribution for obtaining the normal background signal intensity (mean value $\pm$ 3SD) of the solution. Such normal background range was applied to the metal artifact image dataset to determine the thresholding level. All signal values outside this normal range were calculated as susceptibility artifacts from the metal implants. The quantitative image quality was evaluated in terms of signal-to-noise ratio (SNR). The appropriate protocol was selected according to ranking score (1-10 points) by sorting the volume of metallic artifact, SNR and specific absorption rate (SAR).

By acquiring the phantom with the 3D T2 SPACE (protocol 1-9) and 2D T2 TSE (protocol 10) at 1.5 T, the results showed that the average metallic artifact volume of protocol 1-10 were  $162.64 \pm 1.88$ ,  $158.30 \pm 1.79$ ,  $157.82 \pm 2.36$ ,  $126.43 \pm 1.22$ ,  $124.87 \pm 0.29$ ,  $122.93 \pm 1.57$ ,  $117.55 \pm 1.03$ ,  $114.82 \pm 1.55$ ,  $112.40 \pm 0.43$  and  $184.89 \pm 1.19$   $\text{cm}^3$  for the stainless-steel and for titanium, the average metallic artifact volume of protocol 1-10 were  $33.80 \pm 1.03$ ,  $32.56 \pm 0.48$ ,  $33.79 \pm 0.90$ ,  $13.39 \pm 0.67$ ,  $13.77 \pm 0.73$ ,  $12.74 \pm 0.48$ ,  $10.89 \pm 0.77$ ,  $11.42 \pm 0.64$ ,  $10.67 \pm 0.71$  and  $38.86 \pm 0.97$   $\text{cm}^3$ . The metal artifacts were highest reduced at protocol 9 by 39.21% for stainless steel and 72.55% for titanium.

In conclusions, using the 3D SPACE pulse sequence, the artifact volume can be effectively reduced by increasing the receiver bandwidth. The appropriate parameters for metallic artifact reduction with highest-ranking scores were protocol 4 and 5 with bandwidth 501 Hz/pixel, flip angle  $100^\circ$  and  $150^\circ$  in both of stainless steel and titanium respectively.

Field of Study: Medical Imaging  
Academic Year: 2018

Student's Signature .....  
Advisor's Signature .....

## ACKNOWLEDGEMENTS

The success of this thesis depends on the contribution of many people. First of all, I wish to express gratitude and deepest appreciation Assistant Professor Dr. Kitiwat Khamwan for his helpful, supervision, guidance, encouragement and invaluable advice during the whole study.

I wish to express gratitude and appreciation to Miss Supada Prakkamakul, M.D., for her help suggestion for this work.

I wish to express the deepest appreciation to Associate Professor Dr. Anchali Krisanachinda, Associate Professor Sivalee Suriyapee and Professor Franco Milano for their valuable suggestion to this study.

I gratefully acknowledge the member of my thesis committee: Associate Professor Dr. Kosuke Mutsubara, for their valuable suggestion and guidance.

I would like to thank technologists and clinical staff at Unit of Magnetic Resonance Imaging, Department of Radiology, King Chulalongkorn Memorial Hospital, Bangkok, Thailand for their kind support in this study.

I also wish to express gratitude to all lecturers and staff in the Master of Science Program in Medical Imaging, Department of Radiology, Faculty of Medicine, Chulalongkorn University for their unlimited teaching throughout whole study.

Last but not least, my gratefulness to every member in my family for their financial supports, valuable encouragement and entirely cares during the course study.

Thanatchaya Lowong

## TABLE OF CONTENTS

	<b>Page</b>
.....	iii
ABSTRACT (THAI) .....	iii
.....	iv
ABSTRACT (ENGLISH).....	iv
ACKNOWLEDGEMENTS .....	v
TABLE OF CONTENTS.....	vi
LIST OF TABLES .....	ix
LIST OF FIGURES .....	xi
LIST OF ABBREVIATION .....	xiv
CHAPTER I INTRODUCTION.....	1
1.1 Background and rationale .....	1
1.2 Research objective .....	3
1.3 Definition .....	3
CHAPTER II REVIEW OF RELATED LITERATURE .....	4
2.1 Theory .....	4
2.1.1 The introduction of nuclear magnetic resonance.....	4
2.1.2 Spatial Encoding.....	6
2.1.3 MRI artifacts.....	10
2.1.4 Pulse sequence for reducing metal artifacts .....	16
2.1.5 MRI Safety concerns.....	20
2.2 Review of related literatures .....	22
CHAPTER III RESEARCH METHODOLOGY .....	25
3.1 Research design .....	25
3.2 Research design model .....	25
3.3 Conceptual framework.....	25



3.4 Research question .....	25
3.5 Materials.....	26
3.6 Methods.....	28
3.7 Data analysis.....	31
3.8 Sample size determination .....	34
3.9 Statistical analysis.....	35
3.10 Outcome measurement.....	35
3.11 Ethical consideration.....	35
3.12 Expected benefit .....	35
CHAPTER IV RESULTS.....	36
4.1 Quality control of MRI scanner.....	36
4.2. Determination of appropriate parameters.....	37
4.3 Verification of volume measurement .....	37
4.4 Metallic artifact volume measurement.....	39
4.5 Image quality evaluation.....	45
4.6 The Specific Absorption Rate (SAR) .....	46
4.7 Appropriate parameter selection.....	47
CHAPTER V DISCUSSION AND CONCLUSIONS .....	49
5.1 Discussion .....	49
5.2 Conclusions .....	54
REFERENCES.....	56
Appendix A: Case record form .....	58
Appendix B: Quality control of MRI scanner.....	60
1. Geometric Accuracy .....	63
2. High contrast spatial resolution.....	65
3. Slice Thickness Accuracy .....	67
4. Slice position accuracy .....	69
5. Image intensity uniformity .....	71
6. Percent signal ghosting .....	73

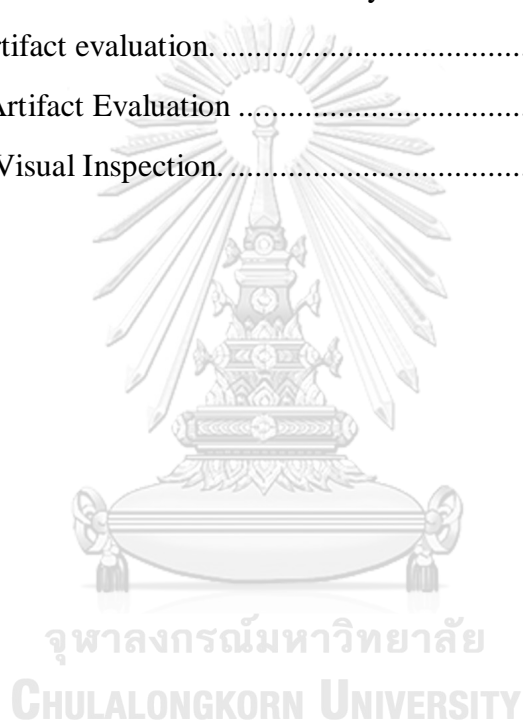
7. Low contrast object Detectability.....	75
8. Image Artifact Evaluation.....	77
9. Magnet Visual Inspection .....	78
Appendix C: Certificate of approval Institutional Review Board (IRB).....	79
VITA.....	80



## LIST OF TABLES

	<b>Page</b>
Table 1. Imaging parameters for phantom study.....	30
Table 2. Parameters for scanning. ....	30
Table 3. The upper and lower threshold for each protocol. ....	32
Table 4. The number of scanning. ....	34
Table 5. Report of MRI 1.5 Tesla testing performance. ....	36
Table 6. Parameters for protocols 1-5. ....	37
Table 7. Parameters for protocols 6-10.....	38
Table 8. The percentage difference between the known and the measured volume. ..	38
Table 9. The results of volume metallic artifact in stainless steel screw.....	39
Table 10. The results of volume of metallic artifact in titanium screw.....	40
Table 11. The results of percent of metallic artifact reduction comparing SPACE sequences (protocol 1-9) to TSE sequences (protocol 10) in stainless steel screw.....	40
Table 12. The results of percent of metallic artifact reduction comparing SPACE sequences (protocol 1-9) to TSE sequences (protocol 10) titanium screw.....	41
Table 13. The results of signal-to-noise ratio (SNR) in stainless steel.....	45
Table 14. The results of signal-to-noise ratio (SNR) in titanium screw.....	45
Table 15. The results of Specific Absorption Rate (SAR) in stainless steel.....	46
Table 16. The results of Specific Absorption Rate (SAR) in titanium. ....	46
Table 17. Ranking score of volume of metallic artifact, SNR and SAR in stainless steel.....	47
Table 18. Ranking score of volume of metallic artifact, SNR and SAR in titanium. .	47
Table 19. Mean signal intensities (Mean $\pm$ SD) in each protocol of the phantom filled with 3.3 g/L, NiCl <sub>2</sub> -6H <sub>2</sub> O and 2.4 g/L NaCl solution. ....	58
Table 20. The volume metallic artifact in stainless steel screw.....	58
Table 21. The volume metallic artifact in titanium. ....	59
Table 22. ACR pulse sequence acquisition parameters.....	62
Table 23. ACR pulse sequence acquisition parameters.....	62

Table 24. Geometric accuracy test results used ACR protocols. ....	64
Table 25. Geometric accuracy test results used routine protocols. ....	64
Table 26. Results of High Contrast Spatial Resolution test. ....	66
Table 27. Slice thickness accuracy test result. ....	68
Table 28. Slice position accuracy test result. ....	70
Table 29. Image intensity uniformity test result. ....	72
Table 30. Pixel value and result of percent signal ghosting test. ....	74
Table 31. The result of low contrast detectability test. ....	76
Table 32. Image artifact evaluation. ....	77
Table 33. Image Artifact Evaluation ....	77
Table 34. Magnet Visual Inspection. ....	78



## LIST OF FIGURES

	Page
Figure 1: Magnetic fields and tissue-metal interactions. (a) Diamagnetic materials. (b) Paramagnetic materials (c) Ferromagnetic materials.....	1
Figure 2: A charged, spinning nucleus creates a magnetic moment which acts like a bar magnet (dipole).....	4
Figure 3: (a) A collection of $^1\text{H}$ nuclei (spinning protons) in the absence of an externally applied magnetic field. The magnetic moments have random orientations. (b) An external magnetic field $B_0$ is applied which causes the nuclei to align themselves in one of two orientations with respect to $B_0$ (denoted parallel and anti-parallel). ....	5
Figure 4: (a) In the presence of an externally applied magnetic field ( $B_0$ ), nuclei are constrained to adopt one of two orientations with respect to $B_0$ . As the nuclei possess spin, these orientations are not exactly at $0^\circ$ and $180^\circ$ to $B_0$ . (b) A magnetic moment precessing around $B_0$ . Its path describes the surface of a cone. ....	6
Figure 5: The slice selection process, illustrated by a plot of the precession frequency versus the slice location. ....	8
Figure 6: Spatial encoding within the selected plane is illustrated using cartoons of the spins (a) after slice selection, (b) upon phase encoding using three phase encoding steps, and (c) after frequency encoding which follows phase encoding. The phase (PE) and frequency (RO) encoding directions are shown on the legend to the right. Relaxation effects are not considered in this figure (9).....	9
Figure 7: $B_0$ field lines of a homogeneous $B_0$ field (a) and deflected by a metal implant (b).....	12
Figure 8: Slice selection using a selection gradient.....	14
Figure 9: Spectral fat suppression (a) and suppression fails near metal (b). ....	15
Figure 10: TSE pulse diagram illustrating the sequence in time of applied gradients, RF pulses, and signal acquisition window. The $90^\circ$ excitation pulse and the first $180^\circ$ refocusing pulse together result in an echo at echo time TE (spin echo sequence). Multiple refocusing pulses may be used to generate multiple spin echoes (turbo spin	

echo). The dashed line indicates the acquisition window during which signal is sampled. ....	16
Figure 11: SPACE used 3D base on turbo spin echo acquisition start with 90 degree pulses and decrease degree of refocusing pulses close to 180-degree for reduced SAR also used 180 degree pulses to maintain SNR received a large number of signal to filling in k-space ( $\theta$ = the flip angle). ....	19
Figure 12: (a) Rods made of Stainless steel (SS), Titanium (Ti), Cobalt-chromium molybdenum (CoCr) and Oxidized zirconium (oxZi). (b) Proton density-weighted (PDw) images with susceptibility artifacts around different metallic rods using different presets of SEMAC-VAT and MAVRIC. ....	23
Figure 13: 3D T2-weighted SPACE imaging as compared with a conventional examination. (a) Conventional axial T2-weighted, (b) Axial T2-weighted SPACE reformat show central disk herniation that is not seen on conventional axial T2-weighted image (a). ....	24
Figure 14: Overview of research design model. ....	25
Figure 15: Conceptual framework. ....	25
Figure 16: MRI 1.5 Tesla, Siemens Medical System: Magnetom, Aera. ....	26
Figure 17: (a) Cylindrical plastic phantom. (b) Cylindrical plastic phantom filled with solution. ....	26
Figure 18: GE workstation (ADW 4.6, General Electric Healthcare, WI, USA). ....	27
Figure 19: (a) Stainless steel (volume 1.05 cm <sup>3</sup> ) and (b) Titanium screws (volume 1.99 cm <sup>3</sup> ). ....	27
Figure 20: ACR MRI phantom. ....	28
Figure 21: The phantom filled with 3.3 g/L, NiCl <sub>2</sub> -6H <sub>2</sub> O and 2.4 g/L NaCl solution, (b) the screw was hung at the middle part of the phantom, (c) positioning of the phantom during MRI acquisition. ....	29
Figure 22: Schematic illustration of the volumetric measurement of metal artifacts. ....	32
Figure 23: The illustrating ROI placements for SNR measurements. Five intensity measurements are made: a large ROI on the image area between 195-205 cm <sup>2</sup> was placed inside the phantom, and standard deviation in the background at 4 locations outside of the image area of the ROI was nearly 10 cm <sup>2</sup> . ....	33

Figure 24: The percent of metallic artifact reduction for both metal implants (stainless steel screw and titanium screw) comparing between T2 SPACE sequences (protocol 1-9) and T2 TSE sequences (protocol 10). ....	42
Figure 25: The images of the metallic artifacts acquired from cylinder plastic phantom filled with solution containing one stainless steel screw evaluated at 1.5 Tesla with T2 weighted TSE sequence (protocol 10), SPACE sequence (protocol 1-9). ....	43
Figure 26: The images of the metallic artifacts acquired from cylinder plastic phantom filled with solution containing one titanium screw evaluated at 1.5 Tesla with T2 weighted TSE sequence (protocol 10), SPACE sequence (protocol 1-9). ....	44
Figure 27: The ranking score of 10 protocols (a) titanium and (b) stainless steel. ....	48
Figure 28: Turbo spin-echo sequence with an echo train length (turbo factor) of 3. ....	50
Figure 29: SPACE pulse sequence. ....	51
Figure 30: Areas under the normal curve that lie between 1, 2 and 3 standard deviations on each side of the mean. ....	53
Figure 31: Sagittal localizer view of ACR MRI Phantom with slice locations for trans axial scans indicated. ....	61
Figure 32: The end to end length and diameter measurement illustrated of the phantom. ....	63
Figure 33: Magnified portion of slice 1 displayed appropriately for visually assessing high contrast resolution. ....	65
Figure 34: ROIs placed for measuring average signal in the ramps. ....	67
Figure 35: Magnified region of slice 1 showing slice thickness signal ramps. ....	68
Figure 36: Images of slice 1 (a) and slice 11 (b) with the pairs of vertical bars from the 45° crossed wedges indicated. ....	70
Figure 37: Images of slice 1 illustrating measurement of slice position error. The arrows indicate the bar length difference measurement that is to be made. (a) The bar on the right is longer, meaning the slice is mispositioned superiorly; this bar length difference is assigned a positive value (+). (b) The bar on the left is longer, meaning the slice is mispositioned inferiorly; this bar length difference is assigned a negative value (-). ....	70

Figure 38: (right) ROI placement for low signal-value, (left) ROI placement for HIGH signal-value.....	71
Figure 39: Image of slice 7 illustrating ROI placements for percent-signal ghosting measurements. ....	73
Figure 40: Image of slice 11 showing the circle of low contrast objects for the low-contrast object detectability test. ....	75





## LIST OF ABBREVIATION

ABBREVIATION	TERMS
ACR	American College of Radiologists
$B_0$	Main magnetic field
$B_1$	Radio-frequency field strength
FID	Free induction decay
FOV	Field of view
FSE	Fast spin echo
GPE	Phase encoding gradient
GRE	Gradient echo
GRO	Read-out gradient
GSS	Slice selection gradient
IR	Inversion recovery
MARS	Metal artifact reduction sequence
MRI	Magnetic resonance imaging
MSVAT	Multiple Slab acquisition
ms	millisecond
NSA	Number of signal average
PD	Proton density
Px	Pixel
QC	Quality control
RF	Radiofrequency
ROI	Region of interest
SE	Spin echo
SEMAC	Slice encoding for metal artifact correction
SPACE	Sampling perfection with application optimized contrasts using different flip angle evolutions
SS	Stainless steel
STIR	short-tau inversion recovery

ABBREVIATION	TERMS
T	Tesla
T1	Longitudinal relaxation
T2	Transverse relaxation
T2*	T2 star
TE	Echo time
Ti	Titanium
TR	Repetition time
TSE	Turbo spin echo
VAT	View angle tilting



## CHAPTER I

### INTRODUCTION

#### 1.1 Background and rationale

Magnetic resonance imaging (MRI) examination consists of several diagnostic scans, each of which results in images of a specific contrast between different tissues. MRI is widely used for clinical evaluation such as in neurology, oncology, cardiology, and orthopedics (1). In particular, orthopedic surgeons require imaging studies in postoperative patient with metal implants. The presence of metal in an anatomic area of interest has proved a difficult and annoying problem for radiologists (2). Imaging assessment of these patients is often limited to plain film x-ray in clinical practice. This limitation is due to metal-induced susceptibility artifacts inherent in MRI and beam hardening artifacts inherent in computed tomography (CT) (3). These artifacts can severely reduce image quality and thus confine the capability in clinical diagnosis.

The behavior of an element in a magnetic field depends on its magnetic property and its susceptibility. Basically, there are three general types of materials with respect to magnetic susceptibility as illustrated in Figure 1.

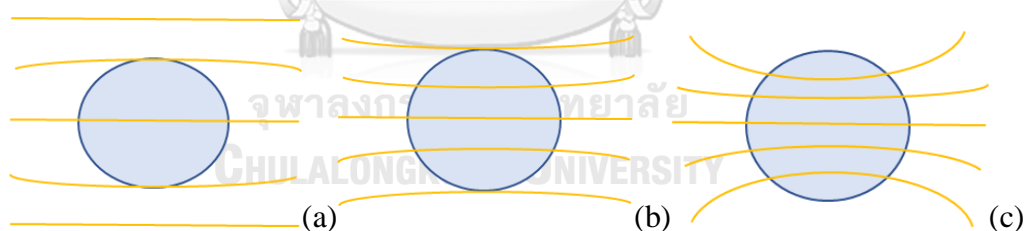


**Figure 1:** Magnetic fields and tissue-metal interactions. (a) Diamagnetic materials. (b) Paramagnetic materials (c) Ferromagnetic materials.

Figure 1(a) depicts a diamagnetic material such as water creates a weak induced magnetic field in the opposite direction to the external magnetic field ( $B_0$ ). Figure 1(b) shows paramagnetic elements like titanium and the Figure 1(c) illustrates the ferromagnetic element iron induced a field in the same direction as  $B_0$ . Unlike the paramagnetic field, ferromagnetic materials also demonstrate greater magnetic susceptibility than paramagnetic materials (4).

Most human tissues are diamagnetic caused weakening of the magnetic field, in contrast to the paramagnetism or ferromagnetism displayed by most modern orthopedic implants. These differences in magnetic susceptibility cause artifact by two principal phenomenons, i.e. accelerated dephasing and signal misregistration. Both of dephasing and misregistration create areas of signal void on the final MR image. Misregistration also causes signal pileup, geometric distortion, and failure of fat suppression.

Practical methods to reduce metal-induced artifact in MR imaging can be done as followings: placing metal implants parallel to the main magnetic field, using lower MR field strength as both of magnetization and inhomogeneity are directly proportional to field strength, i.e. greater magnetization and therefore greater artifact would be expected at 3T than 1.5T, choosing spin echo (SE) sequences rather than gradient echo sequences, increasing bandwidth, and applying a large image matrix and thin slice thickness.

Fast Spin Echo (FSE) or Turbo Spin Echo (TSE) uses of spin-echo sequences corrected for dephasing caused by inhomogeneity and therefore is preferred over gradient-echo sequences for imaging near metal prostheses (5). Spin echo is a two-dimensional (2D) MR pulse sequence, repeated in multiple planes. Although these sequences have excellent tissue contrast and high in-plane spatial resolution, their validity is adversely affected by relatively thick slices and intersection small gaps. Moreover, voxels are not isotropic and multi-planar reformations, therefore, cannot be performed without loss of image quality (1).

Recently, the new MR pulse sequence namely Sampling Perfection with Application Optimized Contrasts using Different Flip Angle Evolutions (SPACE) was introduced in year 2015. This is an innovative 3D-fast (turbo) spin echo acquisition based on true isotropic 3D data records with high resolution. With voxel size less than  $1\text{ mm}^3$ , it can dramatically reduce the intra-voxel dephasing caused by magnetic susceptibility. Additionally, they enable for multi-planar reformation (MPR) if isotropic voxels are used, allowing for an evaluation in any orientation following a single acquisition. As a result, this could be eliminated the need to repeat sequences with identical tissue contrast in multiple planes (6). To our best knowledge, there is no

previous reports regarding the metallic artifact reduction in MR lumbar spine using SPACE pulse sequence before.

## 1.2 Research objective

To determine the 3D T2 SPACE parameters for reducing the metallic artifact in MR lumbar spine 1.5T.

## 1.3 Definition

**MRI:** a non-invasive imaging technology that produces three dimensional detailed anatomical images without the use of damaging radiation. It is often used for disease detection, diagnosis, and treatment monitoring. It is based on sophisticated technology that excites and detects the change in the direction of the rotational axis of protons found in the water that makes up living tissues.

**Turbo Spin Echo:** Fast spin echo (FSE) imaging, also known as Turbo spin echo (TSE) imaging, are commercial implementations of the RARE (Rapid Acquisition with Refocused Echoes) technique originally described by Hennig et al in 1986. The FSE/TSE pulse sequence superficially resembles a conventional spin-echo (CSE) sequence in that it uses a series of 180° refocusing pulses after a single 90° pulse to generate a train of echoes.

**Sampling Perfection with Application Optimized Contrasts using Different Flip Angle Evolutions (SPACE):** SPACE sequence is single slab 3D TSE sequence with slab selective, variable excitation pulse. This sequence enables acquisition of high-resolution 3D datasets with contrasts similar to those obtained from 2D T2-weighted, T1-weighted, proton density and dark fluid protocols at 1.5T and 3T within a clinically acceptable timeframe and without SAR limitations.

**Susceptibility artifacts:** a variety of MRI artifacts that share distortions or local signal change due to local magnetic field inhomogeneities from a variety of compounds. They are especially encountered while imaging near metallic orthopedic hardware or dental work and result from local magnetic field inhomogeneities introduced by the metallic object into the otherwise homogeneous external magnetic field  $B_0$ . These local magnetic field inhomogeneities are a property of the object being imaged, rather than of the MRI unit.

## CHAPTER II

### REVIEW OF RELATED LITERATURE

#### 2.1 Theory

##### 2.1.1 The introduction of nuclear magnetic resonance

The fields of NMR and, by extension, MRI, are based on the interaction of nuclear spin with an external magnetic field. The word “magnetic” is used to describe the various magnetic fields that are involved in the formation of image. The word “resonance” refers to the need to match the oscillating radiofrequency field ( $B_1$ ) to the precession frequency ( $\omega_0$ ) of a nuclear spin.

Nuclei with an odd number of protons and neutrons possess a property called spin. In quantum mechanics spin is represented by a magnetic spin quantum number. Spin can be visualized as a rotating motion of the nucleus about its own axis. As atomic nuclei are charged, the spinning motion causes a magnetic moment in the direction of the spin axis. This phenomenon is shown in Figure 2. The strength of the magnetic moment is a property of the type of nucleus. Although many nuclei possess spin, and can therefore be studied using NMR, clinical MRI applications focus on the hydrogen ( $^1\text{H}$ ) nucleus (containing a single proton), as its large natural abundance and sensitivity make it the easiest to detect and observe within the human (7).

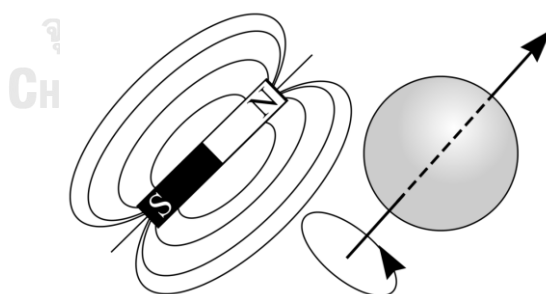


**Figure 2:** A charged, spinning nucleus creates a magnetic moment which acts like a bar magnet (dipole).

Consider a collection of  $^1\text{H}$  nuclei (spinning protons) as in Figure 3a. In the absence of an externally applied magnetic field, the magnetic moments have random orientations. However, if an externally supplied magnetic field  $B_0$  is imposed, the magnetic moments have a tendency to align with the external field (Figure 3b).

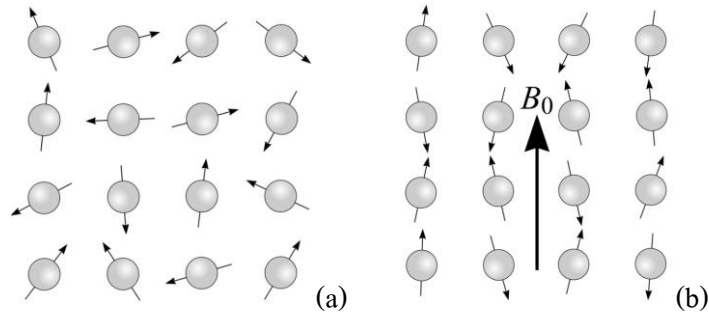


**Figure 3:** (a) A collection of  $^1\text{H}$  nuclei (spinning protons) in the absence of an externally applied magnetic field. The magnetic moments have random orientations. (b) An external magnetic field  $B_0$  is applied which causes the nuclei to align themselves in one of two orientations with respect to  $B_0$  (denoted parallel and anti-parallel).

The magnetic moments or spins are constrained to adopt one of two orientations with respect to  $B_0$ , denoted parallel and anti-parallel. The angles subtended by these orientations and the direction of  $B_0$  are labeled  $\theta$  in Figure 4a. The spin axes are not exactly aligned with  $B_0$ , they precess around  $B_0$  with a characteristic frequency (7) as shown in Figure 4b.

The relationship between the strength of a magnetic field ( $B_0$ ) and the precession frequency ( $\omega_0$ ), of an individual spin as following:

$$\omega_0 = \gamma B_0 \quad (2.1)$$

$\gamma$  is a constant known as the gyromagnetic ratio of the nucleus. The precession frequency ( $\omega_0$ ), is also known as the Larmor frequency. For a hydrogen nucleus,  $\gamma_{\text{H}} = 4257 \text{ Hz/Gauss}$ . Thus at 1.5 Tesla (15,000 Gauss),  $F = 63.855 \text{ Megahertz}$  (8).

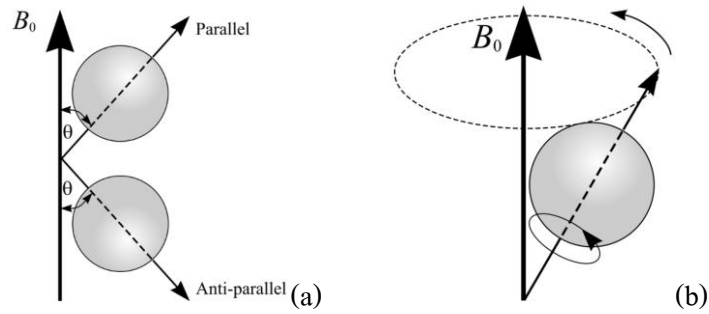


**Figure 4:** (a) In the presence of an externally applied magnetic field ( $B_0$ ), nuclei are constrained to adopt one of two orientations with respect to  $B_0$ . As the nuclei possess spin, these orientations are not exactly at  $0^\circ$  and  $180^\circ$  to  $B_0$ . (b) A magnetic moment precessing around  $B_0$ . Its path describes the surface of a cone.

### 2.1.2 Spatial Encoding

The gradient fields perform three primary functions: slice selection, frequency encoding, and phase encoding. Each of these functions utilizes one or more gradient lobes. A gradient lobe is a single gradient pulse shape that starts and ends with zero amplitude. The pulse sequence consists of a combination of gradient lobes, along each axis, played in a particular order to achieve spatial localization. In general, the following steps are executed: RF excitation with through-plane section selection (called slice selection), frequency encoding and phase encoding for in-plane spatial localization, accompanied by data acquisition. The following sub-sections highlight the role of the imaging gradients for slice selection and spatial encoding (9).

#### 2.1.2.1 Slice Selection

A slice selection gradient is always used concurrently with a spatially selective RF pulse, to achieve the desired spatial localization. This gradient is applied perpendicular to the direction dictated by the desired plane. For convenience, this discussion assumes axial slices, where the gradient is applied along the magnet bore, in the physical  $z$ -direction. The amplitude ( $G_z$ ) of the slice selection gradient is related to the slice thickness ( $\Delta z$ ) and the RF bandwidth ( $\Delta\omega_{RF}$ ) by the following relationship:



$$G_z = \frac{2\pi}{\gamma} \frac{\Delta\omega_{RF}}{\Delta z} \quad (2.2)$$

For a fixed RF bandwidth, the slice thickness is increased by decreasing the amplitude of the slice selection gradient. Figure 5 shows the relationship between the slice selection gradient amplitude and the desired slice thickness.

The imaging plane can be selected at a location away from the isocenter. In this case, the slice offset from the isocenter,  $\partial z$ , is obtained by shifting the carrier frequency of the RF pulse by an amount,  $\partial\omega_{RF}$ , given by:

$$\frac{\partial z}{\partial\omega_{RF}} = \frac{\Delta z}{\Delta\omega_{RF}} \quad (2.3)$$

This relationship assumes a spatially uniform gradient field. Non-linearity away from the magnet isocenter can cause the selected slice to be distorted, somewhat like a potato-chip. Other spatial distortions can result from susceptibility variations in the sample, which can perturb the local gradient fields.

The slice-selection gradient, applied concurrent with the RF excitation pulse, can cause phase dispersion of the transverse magnetization across the slice profile. To avoid the signal loss associated with the phase dispersion, a rephasing gradient lobe is usually applied after the slice selection gradient. The slice rephasing lobe is designed to have opposite polarity with respect to the slice selection gradient lobe, and gradient area equal to the area of the slice selection gradient starting from the isodelay point of the RF pulse. Refocusing RF pulses usually do not require rephasing gradients as the phase accumulated in the first half of the refocusing pulse is cancelled during the latter half. In the case of refocusing pulses, however, the slice selection gradient is usually straddled by crusher gradients on either side, which preserve the spin echo while selectively dephasing the FID and stimulated echoes (9).

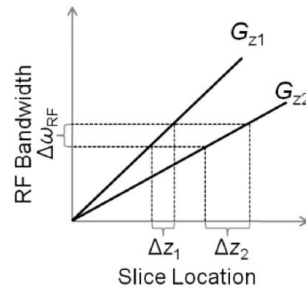


**Figure 5:** The slice selection process, illustrated by a plot of the precession frequency versus the slice location.

#### 2.1.2.2 Frequency Encoding

A linear field gradient can be used to spatially encode NMR signals along the direction of the gradient by assigning a unique precession frequency to each spin isochromatic, depending upon its spatial location within the object. The acquired time-domain NMR signals will therefore contain a range of frequencies, which can be revealed through an inverse Fourier transform. The applied gradient is referred to as the frequency encoding gradient, and the process is called frequency encoding. As the acquisition of the signal is commonly timed to coincide with the application of this gradient, the frequency encoding gradient is also referred to as the readout gradient. Frequency encoding can be applied along any axis, and typically varies with the type of acquisition. In commonly used pulse sequences, the gradient is applied along a set of parallel lines (commonly called phase encoding) (10).

#### 2.1.2.3 Phase Encoding

In order to form an image, it is necessary to accomplish spatial localization in two dimensions. It is not possible to apply frequency encoding independently in two spatial directions, so phase encoding is used along the second dimension. The phase encoding gradient is usually applied right before the frequency encoding gradient, and along a different direction. In MRI, the phase encoding gradient is applied several times within an imaging experiment, with varying amplitudes, while keeping the duration of the gradient lobe the same in all cases. As the gradient area changes, the linear phase variation also changes. The linear phase variation is shown schematically in Figure 6.

The spins contributing to the transverse magnetization are aligned immediately after the slice selection (Figure 6a). Several phase encoding “steps” are needed to acquire the information necessary for the creation of an image (Figure 6b). The acquired data contains information that is a composite of both, frequency and phase encoding (Figure 6c), and this two-dimensional map is called the  $k$ -space map. A two-dimensional MR image can be reconstructed from the acquired information.

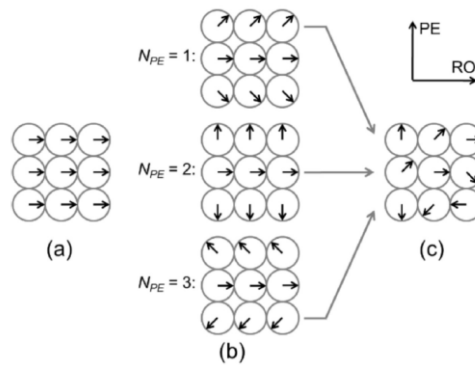


**Figure 6:** Spatial encoding within the selected plane is illustrated using cartoons of the spins (a) after slice selection, (b) upon phase encoding using three phase encoding steps, and (c) after frequency encoding which follows phase encoding. The phase (PE) and frequency (RO) encoding directions are shown on the legend to the right. Relaxation effects are not considered in this figure (9).

### 2.1.3 MRI artifacts

There are a variety of artifacts that can appear in MR images. There are many different causes for artifacts, including equipment malfunctions and environmental factors. However, most artifacts occur under normal imaging conditions and are caused by the sensitivity of the imaging process to certain tissue characteristics such as motion and variations in composition (11).

An artifact is something that appears in an image and is not a true representation of an object or structure within the body. Most MRI artifacts are caused by errors in the spatial encoding of RF signals from the tissue voxels. This causes the signal from a specific voxel to be displayed in the wrong pixel location. This can occur in both the phase-encoding and frequency-encoding directions. Errors in the phase-encoding direction are more common and larger, resulting in bright streaks or ghost images of some anatomical structures. Motion is the most common cause, but the aliasing effect can produce ghost images that fold over or wraparound into the image. Errors in the frequency-encoding direction are limited to a displacement of just a few pixels that can occur at boundaries between fat and not fat tissues in which most of the protons are contained in water. In this thesis we focus on magnetic susceptibility and metal artifacts (11).

#### 2.1.3.1 Magnetic susceptibility and metal artifacts

Magnetic susceptibility corresponds to the internal magnetization of a tissue resulting from the interactions with an external magnetic field. When two tissues with different magnetic susceptibilities are juxtaposed, it causes local distortions in the magnetic field. There are such natural interfaces between air and tissue or between trabecular bone and tissues (11).

These static field inhomogeneities ( $T2^*$ ) create dephasing and frequency shifts of nearby spins. This results in artifacts in the MR image, mostly a loss of signal, but also a distortion of the image. The presence of any metal (ferromagnetic or not) causes large distortions in the magnetic field and significant susceptibility artifacts. The range of signal loss depends on the metal and on the pulse sequence (spin echo, gradient echo). The explanations for this signal loss are the local field inhomogeneities ( $T2^*$ ) which accelerate transverse relaxation and signal decay, the

magnetic field distortion so that there is a precessional frequency shift. When the slice selection is performed, resulting in an absence of spin excitation and an absence of signal. When the signal is acquired and the readout gradient is applied, resulting in a shift of spatial localization which causes a signal loss and/or image distortion (11).

For ferromagnetic materials, magnetization may persist even in absence of the applied magnetic field. For other materials, the magnetization  $M$  is linearly dependent on the applied magnetic field via the relation

$$M = \chi H. \quad (2.4)$$

where  $\chi$  is the magnetic volume susceptibility of the material. The magnetization may have equal or opposed sign to the applied magnetic field for paramagnetic (e.g. air,  $\chi = 4 \times 10^{-7}$ ), and diamagnetic materials (e.g. water,  $\chi = -8 \times 10^{-6}$ ), respectively. The magnetization  $M$  itself contributes to the induced magnetic field  $B_0$ , which is given by

$$B_0 = \mu H = \mu_0(H + M) = \mu_0(1 + \chi)H. \quad (2.5)$$

with  $\mu$  the magnetic permeability of the material and  $\mu_0$  the magnetic permeability of vacuum.

As different tissue materials are at different positions within the scanner, the values of  $M$  and  $B_0$  will depend on the position ( $\vec{r}$ ) as well. The precession frequency  $f_0$  of hydrogen nuclei is dependent on the position as it is directly proportional to the spatially varying induced magnetic field  $B_0$ :

$$f_0(\vec{r}) = \gamma B_0(\vec{r}). \quad (2.6)$$

Ideally, a linear gradient, e.g. the read-out gradient  $G_{\text{READ}}$ , induces a linear variation of the magnetic field in the  $m$  direction (constant  $dB_0/dm$ ), which results in a linear variation of the precession frequency  $f_0$  as a function of the position. However, the local variations in  $B_0$  lead to additional precession frequency deviations (11).

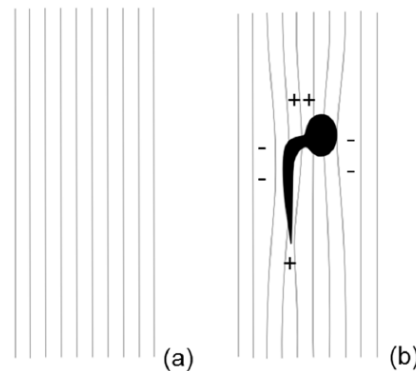


**Figure 7:**  $B_0$  field lines of a homogeneous  $B_0$  field (a) and deflected by a metal implant (b).

The magnetization of the implant amplifies the  $B_0$  field in the metal, which is represented by the condensed field lines. The  $B_0$  field strength increases where the field lines enter and leave the implant, i.e. at the two magnetic poles of the magnetized implant but decreases at the left and right side of the implant, resulting in a dipole character of the induced field (11).

The majority of metal implants are strongly paramagnetic. Placed in the MRI scanner, the metal causes  $B_0$  inhomogeneities that lead to substantial spatial variations of the spin precession frequency  $f_0$ . The metal leads to an increased  $B_0$  field inside the metal, which may be represented by an increased density of magnetic field lines (Figure 7). With this deflection, the field lines are condensed where they enter and leave the implant, i.e. at the two magnetic poles at the cranial and caudal ends of the magnetized implant, and dispersed beside the implant, parallel to the field lines, resulting in a dipole character of the induced field. Resonance frequency offsets associated with metal implants can range from a few kHz (titanium) to well over 10 kHz (11).

### Through-plane distortion

Slice selection, which is used in many MRI sequences, employs an RF pulse of a limited selection bandwidth ( $BW_{SEL}$ ) while a selection gradient ( $G_{SEL}$ ) is applied. With a homogeneous  $B_0$  field and linear gradients, this technique results in a straight slice of excited spins with slice thickness (STK):

$$STK = \frac{BW_{SEL}}{\gamma \times G_{SEL}}. \quad (2.7)$$

However, susceptibility induced field inhomogeneities cause spatial frequency variations, leading to a distortion of the excited slice. Signal is selected if it satisfies the excitation condition:

$$|\gamma \cdot \Delta s \cdot G_{SEL} + \gamma \cdot \Delta B_0(\vec{r})| < BW_{SEL}/2, \quad (2.8)$$

where  $\Delta s$  is the offset in the through-plane direction from the intended slice center. From Eq. 2.8, it can be seen that the through-plane distortion of the slice is given by:

$$\Delta s = -\Delta B_0(\vec{r}) / G_{SEL} \quad (2.9)$$

The through-plane distortion depends on the ratio between the  $B_0$  field inhomogeneity and the selection gradient ( $G_{SEL}$ ) strength. By increasing the selection gradient strength, the relative influence of the susceptibility induced frequency deviations reduces compared to the linear frequency variation induced by the gradient. Practically, the selection gradient may be increased by using thin slices. Alternatively, to maintain the slice thickness, the selection bandwidth may be increased as well, by shortening the RF pulse duration. This usually leads to increased SAR, as achieving an equal flip angle within a shorter RF pulse duration requires a higher  $B_1$  amplitude (11).

### In-plane distortion

In-plane, the location of the signal is determined by frequency encoding in the  $m$  direction and phase encoding in the orthogonal  $p$  direction. The read-out gradient  $G_{READ}$  applied during frequency encoding induces a linear frequency variation, causing each position in the gradient direction to correspond to a unique frequency. Susceptibility induced field variations lead to frequency deviations that disturb the frequency encoding process, and cause displacement of signal in the  $m$  direction by a distance  $\Delta m$ :

$$\begin{aligned} \Delta f_0(\vec{r}) &= -\gamma G_{READ} \cdot m + \gamma \Delta B_0(\vec{r}) = \gamma G_{READ} \left( m + \frac{\Delta B_0(\vec{r})}{G_{READ}} \right) \\ &= \gamma G_{READ} (m + \Delta m). \end{aligned} \quad (2.10)$$

The displacement in the read-out direction is then given by:

$$\Delta m = \Delta B_0(\vec{r})/G_{\text{READ}}. \quad (2.11)$$

Similar to slice distortion, distortion in the frequency encoding direction may be reduced by applying a strong frequency encoding gradient, which reduces the relative influence of the susceptibility induced frequency deviations (Eq. 2.11). In practice, a strong frequency encoding gradient may be obtained by selecting a limited field of view (FOV) in the frequency encoding direction. Alternatively, if the FOV is maintained, using a stronger frequency encoding gradient increases the total frequency dispersion of spins, and requires a larger read-out bandwidth to acquire all signals from the FOV. Hence, the acquired noise also comprises a wider frequency range, and this reduces the SNR (11).

A linear gradient causes spin to precess at linearly increasing frequency  $f_0$  with increasing spatial position  $s$  (Figure 8a). Adjacent RF bands are used to excite and refocus adjacent straight slices (colored bands, Figure 8b). Susceptibility induced  $f_0$  deviation leads to distortion of the selected slice (red, green, purple in Figure 8c,d). Increasing the selection gradient strength reduces the relative influence of susceptibility on the resonance frequency  $f_0$  (Figure 8e and 8f). In the illustrated case, the RF bandwidth is also increased. Alternatively, at the original RF bandwidth, stronger selection gradients lead to selection of thinner slices (11).

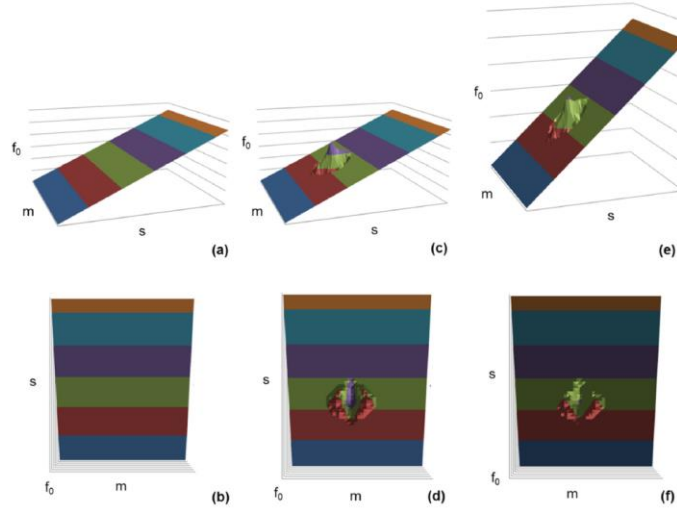


**Figure 8:** Slice selection using a selection gradient.



### Signal intensity errors

Signal displacement leads to geometry distortion and may result in blurring. As some imaged signal is displaced onto other signal, the signal intensity is often disturbed as well, leading to signal pile-up and signal voids. Slice profile distortions, including thickness variations and even disjunct regions of excited signal, also lead to geometry distortion and signal intensity variations. In a gradient echo or fast field echo (FFE), strong local variations of the resonance frequency may cause intra-voxel dephasing, leading to signal voids (11).

### Fat suppression issues

Finally, susceptibility variations may also cause issues with fat suppression. The precession frequencies of hydrogen atoms in fat and in water differ by 3.4 ppm. Spectral fat suppression techniques such as Spectral Presaturation with Inversion Recovery (SPIR) or SPectral Attenuated Inversion Recovery (SPAIR) use this difference to selectively saturate the hydrogen signal of fat (Figure 9a). However, metal induced  $f_0$  deviations are typically much larger than the 3.4 ppm chemical frequency shift of fat with respect to water. This renders spectral fat suppression techniques unreliable near metal implants (Figure 9b).

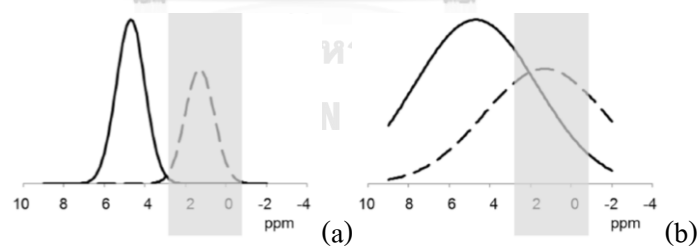


**Figure 9:** Spectral fat suppression (a) and suppression fails near metal (b).

Hydrogen atoms in fat (dashed line) resonate at a slightly different frequency compared to hydrogen atoms in water (solid line), the chemical frequency shift of fat with respect to water being 3.4 ppm. Fat signal can be suppressed using a presaturation RF pulse with a frequency band that includes fat signal only (grey). Spectral fat suppression fails near metal, because the metal induced  $f_0$  deviations are typically much larger than the chemical frequency shift of fat with respect to water. Hence, not all fat signal is suppressed and some water signal is suppressed (11).

## 2.1.4 Pulse sequence for reducing metal artifacts

### 2.1.4.1 Turbo Spin Echo

In Turbo Spin Echo (TSE), also known as Fast Spin Echo (FSE), an excitation is followed by multiple refocusing pulses to induce multiple echoes. This refocusing pulse rotates the spins along an axis that is orthogonal to the rotating axis during excitation, to reduce accumulating effects of imperfections in the  $180^\circ$  pulses. The time interval between two echoes of a TSE echo train is referred to as the echo spacing. In TSE, the TE value is commonly assigned to the echo that has the main contribution to the overall signal in the image, which is the sample in the center of k-space. Figure 10 presents the sequence in time of applied gradients and RF pulses in SE or TSE, as well as the timespan when RF signal is acquired, the acquisition window (11).

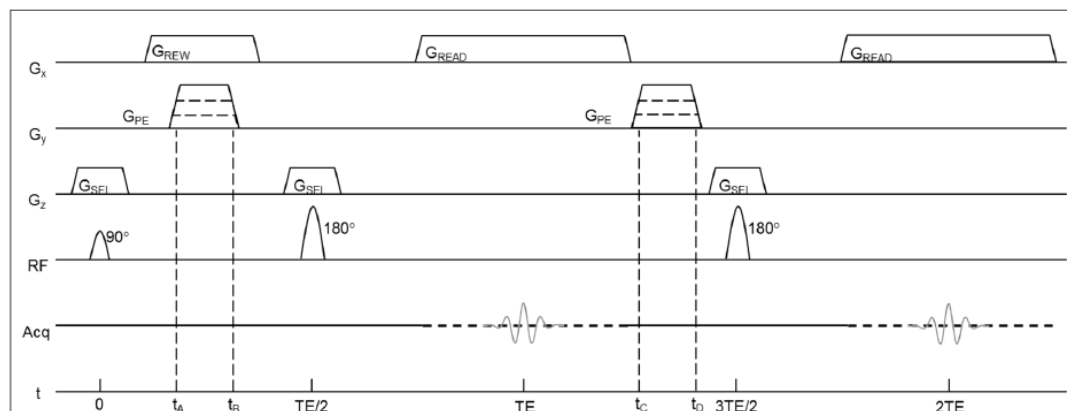


**Figure 10:** TSE pulse diagram illustrating the sequence in time of applied gradients, RF pulses, and signal acquisition window. The  $90^\circ$  excitation pulse and the first  $180^\circ$  refocusing pulse together result in an echo at echo time TE (spin echo sequence). Multiple refocusing pulses may be used to generate multiple spin echoes (turbo spin echo). The dashed line indicates the acquisition window during which signal is sampled.

FFE suffers from signal dephasing due to local  $\Delta B_0$  variations, while TSE is much less sensitive to such dephasing effects. As the strongest  $\Delta B_0$  variations are found close to the metal, TSE enables imaging closer to the implant than FFE. Hence, TSE is commonly used when scanning near metal.

The remaining susceptibility artifacts in high-bandwidth TSE include a variety of effects that can be quite significant, including residual displacement, signal pileups and signal voids. It is important to note the difference between displacement and extent of the artifact, as many small displacements of multiple signals throughout the image may together constitute substantial artifacts that cover a much larger region (11).

### **In-plane distortion in conventional TSE**

During readout, off-resonance signal disturbs the frequency encoding process. The displacement is determined by the maximum field deviation and the read-out gradient. The read-out gradient is usually about 20 mT/m. Using Off-Resonance Suppression (ORS), the field deviation where signal is selected may be up to  $\Delta B_0 = 0.2$  mT, which thus corresponds to an in-plane displacement on the order of 10 mm. When ORS is not used, the in-plane displacement may be much larger (11).

### **Signal voids due to incomplete spectral coverage in TSE**

When using ORS, the total spectral coverage in TSE is limited, and signal outside this spectral range is not imaged, which may lead to signal voids. In practice, including frequency deviations up to 5 kHz is enough to cover most of the signal near titanium implants. Near stainless steel, the frequency deviation will be so large that signal voids are left as a consequence of the modified slice selection process only (11).

### **Signal voids due to insufficient frequency encoding**

Any MRI technique that uses frequency encoding suffers from in-plane distortions as soon as the frequency range of the signal is of the order of or larger than the bandwidth per pixel during read-out. In more extreme cases, local field gradients in the frequency encoding direction may exceed and counteract the applied frequency encoding gradient.

Particularly in regions where the local gradient is nearly equal and opposite to the read-out gradient, the read-out gradient is nearly cancelled and all signal is mapped onto a single image position, while leaving signal voids elsewhere (12).

#### **2.1.4.2 Sampling Perfection with Application Optimized Contrasts using Different Flip Angle Evolutions (SPACE)**

The contrast properties and inherent insensitivity of spin echo-based sequences to RF and magnetic field inhomogeneities make them a particularly desirable addition to a clinical high field protocol, where susceptibility effects can be quite pronounced. Fast imaging methods, such as Turbo Spin Echo (TSE), use a train of refocusing pulses (the Turbo factor or Echo Train Length (ETL)) to enable multiple phase encoding steps to be carried out after each excitation pulse. The increased RF power deposition can, however, severely limit the coverage possible in multi-slice applications at high field, since power deposition or Specific Absorption Rate (SAR) increases as the square of field strength as well as the square of the flip angle. Additionally, increased saturation and magnetization transfer effects reduce contrast and signal-to noise ratios (CNR and SNR). High resolution 3D acquisitions enable precise characterization and localization of anatomy and pathology, but acquisition times are prohibitively long, and T2-weighted sequences are usually only a viable option in 2D mode. Acquisition speed increases are limited by the length of the echo train (T2 decay restraints) and very long echo trains are generally not possible due to loss of contrast and blurring. To enable high field and 3D imaging with these sequences at 3T and above.

The Sampling Perfection with Application Optimized Contrasts using Different Flip Angle Evolutions (SPACE) has introduced by reduced flip angle refocusing approaches lengthen the usable echo train length, since the complex combination of spin and stimulated echoes introduces a T1 dependence to the signal evolution. Significantly reduced SAR at comparable SNR can be obtained by replacing a constant low flip angle refocusing train by a variable flip angle pulse train designed to produce a constant echo amplitude see Figure 11. Starting the pulse train with higher amplitude pulses and slowly decreasing to approach a constant (“asymptotic”) value, enables acquisition of images with SNR values close to those acquired with 180 degree refocusing pulses, for asymptotic flip angles as low as 60 degrees. This “pseudo steady state” of signal intensities decays slowly due to T1 and T2 effects. It is possible to obtain both an increase in signal intensity and an almost

constant signal from the tissue of interest (e.g. gray matter) for the bulk of the signal acquisition, by using prescribed signal evolutions which include relaxation effects in the calculation of refocusing flip angles.

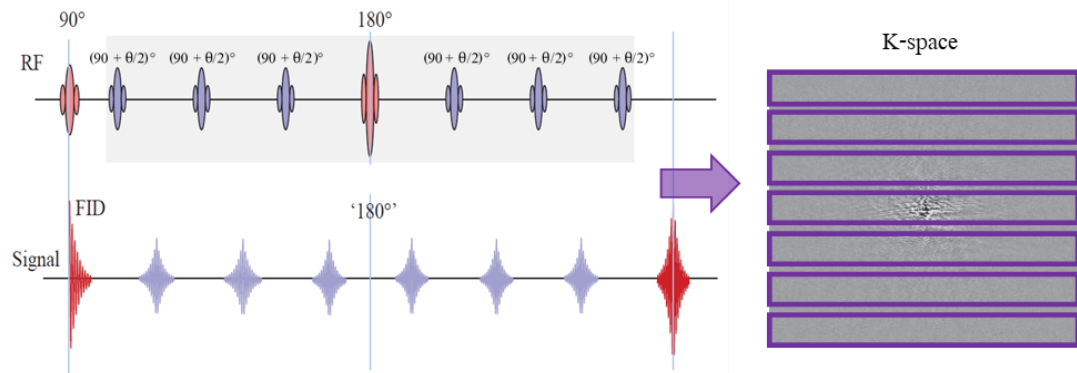


**Figure 11:** SPACE used 3D base on turbo spin echo acquisition start with 90 degree pulses and decrease degree of refocusing pulses close to 180-degree for reduced SAR also used 180 degree pulses to maintain SNR received a large number of signal to filling in k-space ( $\theta$  = the flip angle).

Flip angles need to be optimized for only one tissue of interest (e.g. gray matter in the brain) as the prescribed signal evolutions depend only weakly on the T1 and T2 relaxation times and are therefore similar for many other tissues. Using an initial exponential decay, a constant and then another exponential decay for the prescribed signal evolution produces images in which the contrast is similar to those obtained using conventional T2-weighted Spin Echo sequences. This approach allows very long echo trains and 3D imaging, since the effective T2 of the echo train is longer than the tissue T2 for tissues with long T1s ( $\geq 10 T_2$ ) and acquisition times can be commensurately reduced, or resolution increased (13).

SPACE is an important prerequisite for using T2-weighted 3D imaging - fast (turbo) spin echo acquisition, true isotropic 3D data records with high resolution, voxel size less than  $1 \text{ mm}^3$  can reduce the intra-voxel dephasing caused by magnetic susceptibility. Reduced flip angle refocusing approaches significantly reduced SAR. Increase in signal intensity and an almost constant signal can be obtained by replacing a constant low flip angle refocusing train by a variable flip angle pulse train designed to produce a constant echo amplitude (6).

### 2.1.5 MRI Safety concerns

MR imaging is often the modality of choice to evaluate soft tissues, and as many patients are treated with metal implants, there may be risks involved with an MRI examination or even with having the implant near the MRI scanner, and for some implants an MRI examination is contraindicated. These risks are related to the static magnetic field, the field gradients and the transmitted RF field.

The static magnetic field may exert forces on the implant, which may include translational and rotational forces, if the implant contains ferromagnetic materials. Forces can also result from eddy currents in the metal when the patient moves the body part that contains the implant in the magnetic field. Typically, in highly conducting materials like copper or aluminum, strong eddy currents may be induced by motion of the implant in the magnetic field. Eddy currents in turn induce a local magnetic field which counteracts the motion with respect to the main magnetic field. Both ferromagnetic attraction and eddy currents need to remain limited to avoid painful and potentially dangerous torque and translational forces between the implant and the patient's body (11).

The RF field disposes energy into the patient. The Specific Absorption Rate (SAR) refers to the amount of energy absorbed by the patient during an MRI scan sequence. A distinction is made between global SAR and whole-body SAR which reflects the energy absorbed by the patient's entire body, and local SAR pertaining to potential local elevation of the energy absorption. Each commercially available MRI scanner is equipped with a SAR model that predicts and specifies the whole-body SAR level in W/kg for any defined scan protocol. These model predictions are based on the energy required to transmit the RF field, on calorimetric phantom studies, and on numerical simulations of Maxwell's equations. For head scans, models are available to predict the local SAR (head SAR). By regulation, limitations apply to the SAR level allow 2 W/kg in normal mode for whole-body and 4 W/kg in first level-controlled mode, which requires medical supervision of the patient (14).

Generally, global SAR is more easily estimated than local SAR, as the spatial distribution of the energy in the body may be influenced by many factors. Estimating local SAR becomes increasingly difficult near metal implants due to the interaction of the transmitted RF field and the metal prosthesis, which leads to increased local SAR in the tissue near the implant. Numerical simulations may be used to derive the local SAR distribution (11).

The presence of implants that are categorized as MR-unsafe, such as most pacemakers, cochlear implants and most aneurysm clips, is a contraindication to perform an MRI examination. But many other implants are labeled MR-safe or MR-conditional, meaning that for those implants, the patient is allowed to undergo an MR examination within specified conditions for the static magnetic field, the gradient strength and slew-rate applied during the scan sequences, as well as the SAR (11).

## 2.2 Review of related literatures

**Tao Ai, et al (3)** evaluated the ability of 4 MRI techniques for correcting metallic artifacts using 2D imaging VAT, SEMAC, SEMAC-VAT and 3D imaging MSVAT-SPACE. They used agarose phantoms and tissue phantoms with two commonly used metal implants stainless steel and titanium as well as two volunteers with metal implants were imaged at 1.5T. All phantoms and volunteers were imaged using VAT, SEMAC, SEMAC-VAT and MSVAT-SPACE techniques, as well as 2D and 3D conventional imaging techniques. Each technique was optimized for different image contrast mechanisms. Artifact reduction was quantitatively assessed in the agarose phantoms by volumetric measurement.

They found that the efficacy of susceptibility artifact reduction with different sequence strategies. SEMAC-VAT results in the best metal artifact correction compared with the conventional, VAT and SEMAC techniques in 2D imaging. MSVAT-SPACE shows significantly less metal artifact than conventional techniques in 3D imaging. These new techniques can provide reliable artifact correction across the breadth of conventional image contrasts used in routine orthopedic imaging (T1, T2, PD, and STIR).

According to their results, SEMAC-VAT (2D) and MSVAT-SPACE (3D) demonstrated a consistent, marked reduction of metal artifacts for different metal implants and offered flexible image contrasts (T1, T2, PD and STIR) with high image quality.



**Lukas Filli, et al (15)** compared the degree of artifact reduction with SEMAC-VAT and MAVRIC to determine optimal metal and contrast-specific scan protocols. They used rods made of Stainless steel (SS), Titanium (Ti), Cobalt-chromium molybdenum (CoCr) and Oxidized zirconium (oxZi) for metallic material, then placed rod in the center of the plastic drum phantom filled with copper sulfate solution performed at 3 Tesla (Ingenia; Philips) using Fast spin-echo, SEMAC-VAT and MAVRIC. Two independent readers measured artifacts. They found that stainless steel caused the greatest artifacts, followed by CoCr, Ti, and oxZi regardless of the imaging sequence. There was no optimal scanning protocol for all implant materials. In conclusions, metal artifact reduction techniques such as SEMAC-VAT and MAVRIC need to be tailored to the involved prosthetic material and the applied image contrast weighting.

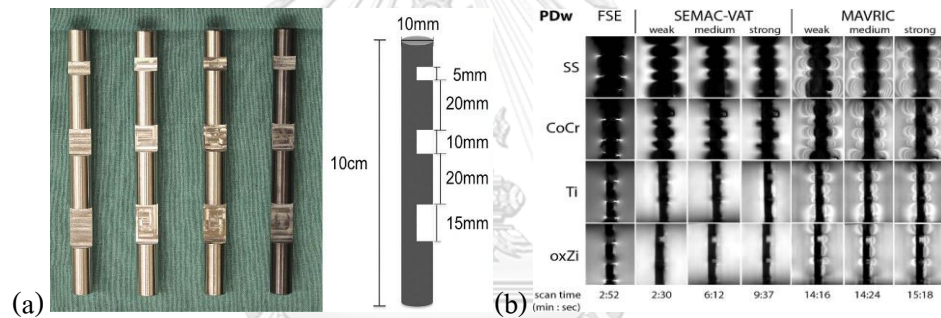


**Figure 12:** (a) Rods made of Stainless steel (SS), Titanium (Ti), Cobalt-chromium molybdenum (CoCr) and Oxidized zirconium (oxZi). (b) Proton density-weighted (PDw) images with susceptibility artifacts around different metallic rods using different presets of SEMAC-VAT and MAVRIC.

**Sayah Anousheh, et al (16)** recently evaluated the effectiveness of a rapid unenhanced lumbar spine MRI protocol using 3D T2-weighted SPACE imaging as compared with a conventional examination. They observed slightly higher sensitivities and comparable specificities of this rapid study over the examination without 3D imaging.

They found that the rapid lumbar MRI protocol with 3D T2-weighted imaging has comparable sensitivities and specificities in diagnosing herniations and neural compromise compared with the conventional examination. They concluded that the use of sagittal T2-weighted SPACE imaging is robust and could decrease scanning times and result in similar accuracies in the evaluation of lumbar spondylosis and neural compromise. Because this rapid protocol can be completed in 15 minutes, it can reduce cost and discomfort for a large subgroup of patients.

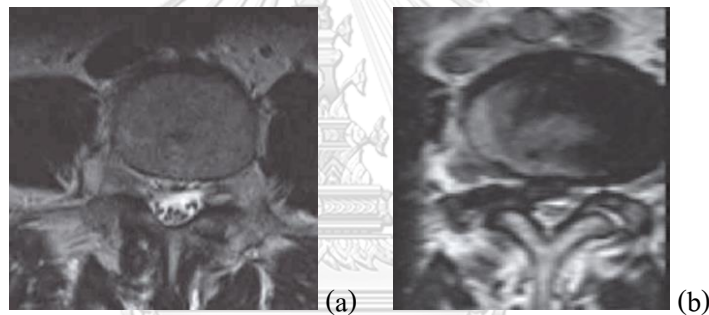


**Figure 13:** 3D T2-weighted SPACE imaging as compared with a conventional examination. (a) Conventional axial T2-weighted, (b) Axial T2-weighted SPACE reformat show central disk herniation that is not seen on conventional axial T2-weighted image (a).

## CHAPTER III

### RESEARCH METHODOLOGY

#### 3.1 Research design

This research was an observational descriptive study.

#### 3.2 Research design model

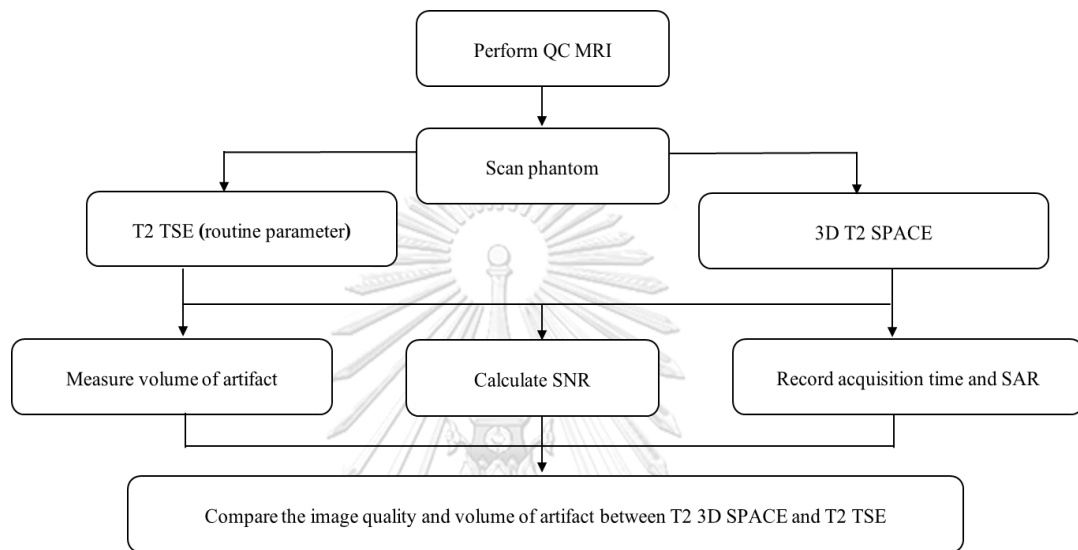


**Figure 14:** Overview of research design model.

#### 3.3 Conceptual framework

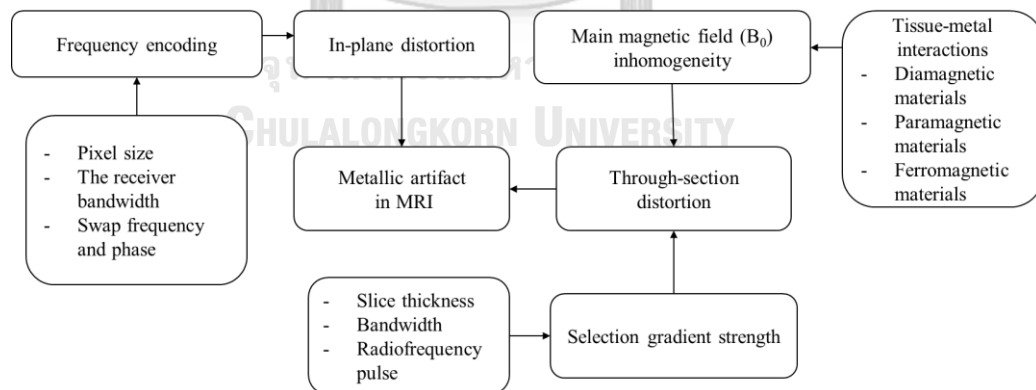


**Figure 15:** Conceptual framework.

#### 3.4 Research question

What are appropriate parameters of 3D T2 SPACE for reducing the metallic artifact in MR lumbar spine?

### 3.5 Materials

#### 3.5.1 MRI 1.5 Tesla, Siemens Medical System model Magnetom, Aera

MRI 1.5 Tesla, with 70 cm magnet bore and in combination with ultra-short system design, digital coil and auto calibration software version E11, was installed at the MRI unit, Department of Radiology, King Chulalongkorn Memorial Hospital in 2012.



**Figure 16:** MRI 1.5 Tesla, Siemens Medical System: Magnetom, Aera.

#### 3.5.2 Cylindrical plastic phantom

Cylindrical plastic phantom filled with 3.3 g/L,  $\text{NiCl}_2 \cdot 6\text{H}_2\text{O}$  and 2.4 g/L NaCl as the same solution in ACR MRI phantom was used to simulate biological conductivity. The dimension of phantom is 21.6 cm for inner diameter, height 18.6 cm, and wall thickness of 3.2 mm.

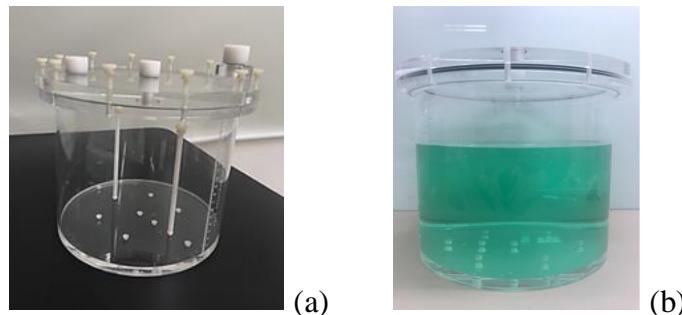


**Figure 17:** (a) Cylindrical plastic phantom. (b) Cylindrical plastic phantom filled with solution.

### 3.5.3 GE workstation (ADW 4.6, General Electric Healthcare, WI, USA)

The histogram tool software on GE workstation (ADW 4.6, General Electric Healthcare, WI, USA) was used for measuring signal intensities, standard deviation and volumetric measurement.



**Figure 18:** GE workstation (ADW 4.6, General Electric Healthcare, WI, USA).

### 3.5.3 Metallic screws

Two different types of metallic screw (stainless steel and titanium) that widely used in orthopedic surgery as illustrated in Figure 19 was used for mimicking the metallic implants in lumbar spine. Stainless steel has length 40 mm, mass 8 g and volume  $1.05 \text{ cm}^3$ . Titanium has length 42 mm, mass 9 g and volume  $1.99 \text{ cm}^3$ . Each metallic screw was suspended at the center of the cylinder plastic phantom.

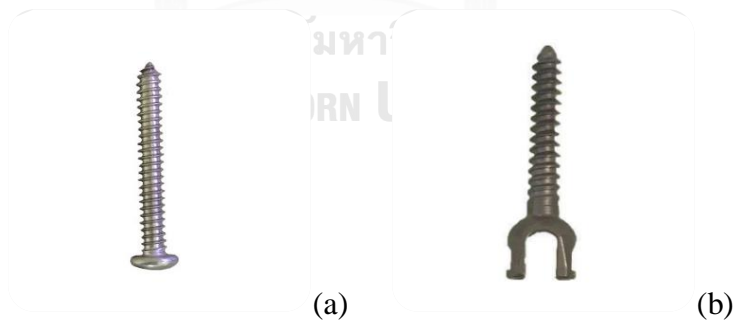


**Figure 19:** (a) Stainless steel (volume  $1.05 \text{ cm}^3$ ) and (b) Titanium screws (volume  $1.99 \text{ cm}^3$ ).

### 3.5.4 ACR MRI phantom



**Figure 20:** ACR MRI phantom.

The ACR MRI accreditation phantom as shown in Figure 20 was used for testing the performance of MR scanner. The phantom is made of acrylic plastic, glass and silicone rubber. The inside length is 148 mm; the inside diameter is 190 mm. It is filled with the solution of nickel chloride and sodium chloride: 10 mM  $\text{NiCl}_2$  and 75 mM  $\text{NaCl}$ . The outside of the phantom has the words “NOSE” and “CHIN” etched into it as an aid to orienting the phantom for scanning. Several structures are designed inside the phantom to facilitate a variety of scanner performance test.

## 3.6 Methods

### 3.6.1 Quality control of MRI scanner

In order to ensure that the MRI scanner has worked properly during data acquisition, the quality control of MRI 1.5 Tesla was performed following ACR manual (2015). The QC testing topics were as followings:

- 3.6.1.1 Geometric accuracy
- 3.6.1.2 High contrast spatial resolution
- 3.6.1.3 Slice thickness accuracy
- 3.6.1.4 Slice position accuracy
- 3.6.1.5 Image intensity uniformity
- 3.6.1.6 Percent signal ghosting
- 3.6.1.7 Low contrast object detectability
- 3.6.1.8 Image artifact evaluation
- 3.6.1.9 Magnet visual inspection

### 3.6.2 The cylindrical phantom acquisition

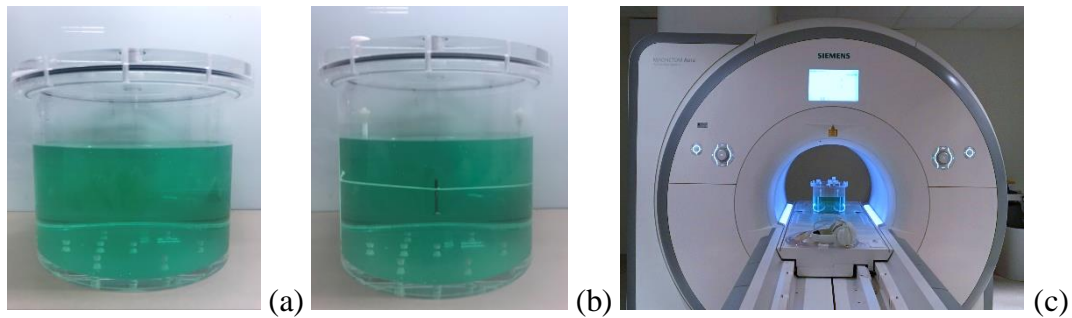


**Figure 21:** The phantom filled with 3.3 g/L,  $\text{NiCl}_2 \cdot 6\text{H}_2\text{O}$  and 2.4 g/L NaCl solution, (b) the screw was hung at the middle part of the phantom, (c) positioning of the phantom during MRI acquisition.

A cylindrical plastic phantom was filled with 2800 cc of 3.3 g/L,  $\text{NiCl}_2 \cdot 6\text{H}_2\text{O}$  and 2.4 g/L NaCl solution in order to represent biological conductivity. A widely used metallic screw for lumbar spine surgery (titanium, stainless steel) was placed at the center of the cylinder plastic phantom as shown in Figure 21. The phantom was scan using MRI 1.5 T model Magnetom Aera manufactured by Siemens Medical Solution. All prepared phantoms were imaged using TSE and SPACE sequences by varying the flip angle of  $100^\circ$ ,  $150^\circ$ ,  $180^\circ$  and bandwidth of 296, 501 and 723 Hz/pixel according to Table 1. Other parameters were kept constantly as shown in Table 2. Totally, there were 10 protocols for investigating the appropriate parameters. The phantom was acquired 3 times in each scanning protocol. The acquisition time and specific absorption rate (SAR) were also recorded. In order to eliminate the bias for data acquisition, the GRAPPA (GeneRalized Autocalibrating Partial Parallel Acquisition) parallel imaging technique was removed from the SPACE pulse sequence.



**Table 1.** Imaging parameters for phantom study.

<b>Pulse sequence</b>	<b>Imaging protocol</b>	<b>Bandwidth (Hz/pixel)</b>	<b>Flip angle (°)</b>
SPACE	Protocol 1	296	100
	Protocol 2	296	100
	Protocol 3	296	100
	Protocol 4	501	150
	Protocol 5	501	150
	Protocol 6	501	150
	Protocol 7	723	180
	Protocol 8	723	180
	Protocol 9	723	180
TSE	Protocol 10	100	150

**Table 2.** Parameters for scanning.

<b>Imaging parameters</b>	<b>TSE</b>	<b>SPACE</b>
TR (ms)	3000	1500
TE (ms)	180	180
Partition thickness (mm)	4	1
FOV (mm)	250×250	250×250
Matrix size	256×256	256×256
Interslice gap (mm)	0	0
Number of slices	20	80
GRAPPA	-	Removed
No. of signals averaged	2	1
Acquisition time (min)	5:31	12:05

The acquired plane was along the long axis of the screw. TR indicates repetition time; TE, echo time; FOV, field of view.



### 3.7 Data analysis

#### 3.7.1 Metallic artifact volume measurement

In order to analyze the volume artifacts, the histogram tool software on GE workstation was used. The volume measurement was calculated according to the steps as followings:

- 1) Determine the normal background range from the phantoms filled with biological conductivity solution.
- 2) Apply a histogram tool to measure the mean signal intensity (SI), standard deviation (SD) and volume of solution ( $Vol_{\text{Solution}}$ ) in the phantom.
- 3) The normal range of signal intensity was then defined as  $\text{mean} \pm 3SD$  for phantom filled with solution. The normal background range can be obtained using equation as followings:

$$\text{Normal background range} = \text{mean SI} \pm 3SD, \quad (3.1)$$

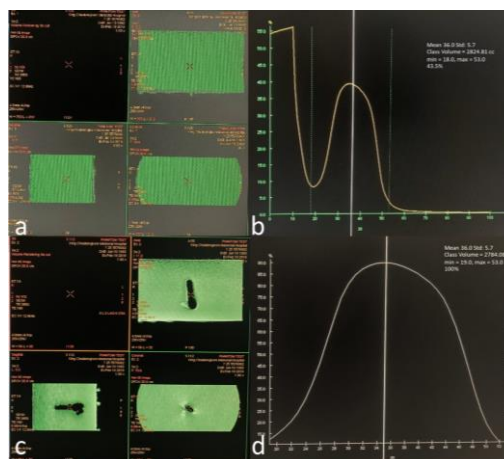
- 4) The calculated normal background range was applied to the image of phantoms with metallic screw using thresholding technique to determine the threshold level. Eventually, the upper and lower threshold levels in each protocol were obtained as in Table 3.
- 5) Signal intensity values outside this normal range were assigned as the susceptibility artifacts.
- 6) A histogram tool was applied again in order to calculate the volume of image dataset of the metal artifact after applying normal background range ( $Vol_{\text{Image artifact}}$ ), and the volume of artifact can be calculated by following equation:

$$\text{Volume of artifact (Vol}_{\text{Artifact}}) = Vol_{\text{Solution}} - Vol_{\text{Image artifact}}, \quad (3.2)$$

**Table 3.** The upper and lower threshold for each protocol.

Pulse sequence	Imaging protocol	Lower threshold	Upper threshold
SPACE	Protocol 1	8.2	35.8
	Protocol 2	9.9	38.1
	Protocol 3	9.6	38.4
	Protocol 4	9.2	36.8
	Protocol 5	9.9	38.1
	Protocol 6	10.3	39.7
	Protocol 7	8.6	37.4
	Protocol 8	9.9	38.1
	Protocol 9	10.9	39.1
TSE	Protocol 10	18.9	53.1

Figure 22 (a-d) depicts the example for schematic of the volumetric measurement of metal artifacts. MR image of phantoms filled with solution (a) with associated histogram analysis (b) was performed within the volume measurement. Mean signal intensity (SI) was 36.0 with standard deviation (SD) of 5.7. The normal range of SI was then defined as mean  $\pm$  3SD for image of phantoms filled with solution. When the normal range was applied into the corresponding MR image of the phantom with metallic implant (c) and associated SI histogram (d), all the pixels with SI outside the normal range (lower threshold = 19 and upper threshold = 53) were subtracted and considered as the metal-induced artifacts.

**Figure 22:** Schematic illustration of the volumetric measurement of metal artifacts.

### 3.7.2 Image quality evaluation

The image quality between TSE routine protocol and T2 3D SPACE in each protocol was evaluated in terms of Signal-to-noise ratio (SNR). The SNR can be calculated using equation as followings:

$$SNR = \frac{\text{mean pixel value inside phantom (exclude artifact)}}{SD \text{ background (outside phantom)}}, \quad (3.3)$$

where mean pixel value inside phantom was measured with in the regions of interest (ROI) inside phantom by excluding the metallic artifact region, and the standard deviation (SD) in the background was measured in the regions of interest (ROI) outside the phantom. There were 4 ROIs for measuring the SD in the background in each protocol as illustrated in Figure 23.

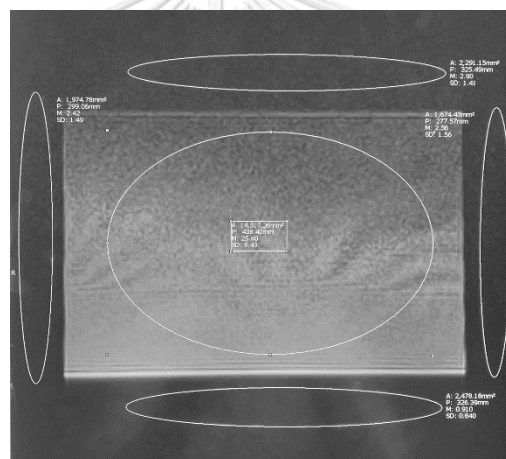


**Figure 23:** The illustrating ROI placements for SNR measurements. Five intensity measurements are made: a large ROI on the image area between 195-205 cm<sup>2</sup> was placed inside the phantom, and standard deviation in the background at 4 locations outside of the image area of the ROI was nearly 10 cm<sup>2</sup>.

### 3.7.3 Optimized parameter selection

The images with 10 protocols were assessed by ranking score (1-10 points) in terms of volume of metallic artifact, signal-to-noise ratio (SNR) and specific absorption rate (SAR). The criteria for scoring are following:

1. The large volume of metallic artifact → low score.
2. The high value of SNR → high score.
3. The high value of SAR → low score.

In order to the appropriate parameter, the score in each topic must be equal or greater than five-point ( $\geq 5$ ).

### 3.8 Sample size determination

The sample size was calculated for number of times for scanning. There were 10 protocols, 2 metallic materials for each protocol were performed in 3 times and the phantom filled with solution was scanned in each protocol 1 time. The total number of scanning was 70 times as shown in Table 4.

**Table 4.** The number of scanning.

Pulse sequence	Imaging protocol	Number of scans (times)		
		Stainless steel	Titanium	Phantoms filled with solution
SPACE	Protocol 1	3	3	1
	Protocol 2	3	3	1
	Protocol 3	3	3	1
	Protocol 4	3	3	1
	Protocol 5	3	3	1
	Protocol 6	3	3	1
	Protocol 7	3	3	1
	Protocol 8	3	3	1
	Protocol 9	3	3	1
TSE	Protocol 10	3	3	1
Total		30	30	10

### **3.9 Statistical analysis**

The results of analysis will be presented in terms of descriptive statistics: Maximum, Minimum, Mean, Standard deviation (SD).

### **3.10 Outcome measurement**

- Volume of metallic artifact
- Acquisition time
- Signal-to-Noise Ratio (SNR)
- Specific absorption rate (SAR)

### **3.11 Ethical consideration**

This study was performed in phantom on MRI 1.5 Tesla at MRI unit, King Chulalongkorn Memorial Hospital. The research proposal has already been approved by Institutional Review Board (IRB) of Faculty of Medicine, Chulalongkorn University (IRB No. 392/61).

### **3.12 Expected benefit**

Obtain appropriate parameters for reducing metallic artifact in MRI lumbar spine based on 3D T2 SPACE pulse sequence at MRI 1.5 Tesla.

## CHAPTER IV

### RESULTS

#### 4.1 Quality control of MRI scanner

The quality control of 1.5 Tesla MRI system was performed following the latest ACR manual published in 2015. The results of geometric accuracy, high contrast spatial resolution, slice thickness accuracy, slice position accuracy, image intensity uniformity, percent signal ghosting, low contrast object detectability, image artifact evaluation and magnet visual inspection are shown in Appendix B. The summarize report of MRI system performance testing is shown in Table 5.

**Table 5.** Report of MRI 1.5 Tesla testing performance.

Location:	King Chulalongkorn Memorial Hospital	
Date:	30 March 2018	
Manufacture:	Siemens Healthcare	
Model	MAGNETOM Aera 1.5 Tesla	
Series number	J11710	
Geometric accuracy		Pass
High contrast spatial resolution		Pass
Slice thickness accuracy		Pass
Slice position accuracy		Pass
Image intensity uniformity		Pass
Percent signal ghosting		Pass
Low contrast object detectability		Pass
Image artifact evaluation		Pass
Magnet visual inspection		Pass

## 4.2. Determination of appropriate parameters

In order to seek the optimized parameter for metallic artifact reduction, the parameters of T2 TSE (routine protocol) and T2 SPACE pulse sequences were adjusted by varying the flip angle at 100°, 150°, 180° and bandwidth of 296, 501 and 723 Hz/pixel. The details of pulse sequence parameters using for scanning the phantom is shown in Table 6 and 7.

## 4.3 Verification of volume measurement

In order to verify the accuracy of software tool on GE workstation for measuring the volume of solution accurately, the known volume of solution was filled into the phantom. It was found that the percentage difference between the known volume and the measured volume was less than 1% for all protocols as shown in Table 8.

**Table 6.** Parameters for protocols 1-5.

Imaging parameters	SPACE				
	Protocol 1	Protocol 2	Protocol 3	Protocol 4	Protocol 5
Bandwidth (Hz/pixel)	296	296	296	501	501
Flip angle (°)	100	150	180	100	150
TR (ms)	1500	1500	1500	1500	1500
TE (ms)	180	180	180	180	180
Slice thickness (mm)	1	1	1	1	1
FOV (mm)	250×250	250×250	250×250	250×250	250×250
Matrix size	256×256	256×256	256×256	256×256	256×256
Interslice gap (mm)	0	0	0	0	0
Number of slices	80	80	80	80	80
GRAPPA	-	-	-	-	-
No. of signals averaged	1	1	1	1	1
Acquisition time (min)	12:05	12:05	12:05	12:05	12:05

**Table 7.** Parameters for protocols 6-10.

Imaging parameters	SPACE				TSE
	Protocol 6	Protocol 7	Protocol 8	Protocol 9	Protocol 10
Bandwidth (Hz/pixel)	501	723	723	723	100
Flip angle (°)	180	100	150	180	150
TR (ms)	1500	1500	1500	1500	3000
TE (ms)	180	180	180	180	180
Slice thickness (mm)	1	1	1	1	4
FOV (mm)	250×250	250×250	250×250	250×250	250×250
Matrix size	256×256	256×256	256×256	256×256	256×256
Interslice gap (mm)	0	0	0	0	0
Number of slices	80	80	80	80	20
GRAPPA	-	-	-	-	-
No. of signals averaged	1	1	1	1	2
Acquisition time (min)	12:05	12:05	12:05	12:05	5:31

**Table 8.** The percentage difference between the known and the measured volume.

Imaging protocol	Known volume of solution (cm <sup>3</sup> )	Measured volume of solution (cm <sup>3</sup> )	Percentage difference
Protocol 1	2800	2809.90	0.35
Protocol 2	2800	2800.01	0.00
Protocol 3	2800	2800.79	0.03
Protocol 4	2800	2798.15	0.07
Protocol 5	2800	2806.55	0.23
Protocol 6	2800	2806.28	0.22
Protocol 7	2800	2804.94	0.18
Protocol 8	2800	2801.56	0.06
Protocol 9	2800	2804.51	0.16
Protocol 10	2800	2801.80	0.06



#### 4.4 Metallic artifact volume measurement

For the stainless-steel screw, the average metallic artifact volume of protocol 1-10 were  $162.64 \pm 1.88$ ,  $158.30 \pm 1.79$ ,  $157.82 \pm 2.36$ ,  $126.43 \pm 1.22$ ,  $124.87 \pm 0.29$ ,  $122.93 \pm 1.57$ ,  $117.55 \pm 1.03$ ,  $114.82 \pm 1.55$ ,  $112.40 \pm 0.43$  and  $184.89 \pm 1.19$  cm<sup>3</sup> as shown in Table 9. For the titanium screw, the average metallic artifact volume of protocol 1-10 were  $33.80 \pm 1.03$ ,  $32.56 \pm 0.48$ ,  $33.79 \pm 0.90$ ,  $13.39 \pm 0.67$ ,  $13.77 \pm 0.73$ ,  $12.74 \pm 0.48$ ,  $10.89 \pm 0.77$ ,  $11.42 \pm 0.64$ ,  $10.67 \pm 0.71$  and  $38.86 \pm 0.97$  cm<sup>3</sup> as shown in Table 10.

By acquiring the phantom with the 3D T2 SPACE (protocol 1-9) at 1.5 Tesla as illustrated in Figure 25 and 26, the metal artifact volume was dramatically reduced when compared to the T2 TSE sequence (protocol 10). The highest percent of metallic artifact was reduced by  $39.21\% \pm 0.16\%$  and  $72.51\% \pm 2.37\%$  in protocol 9 for both of stainless-steel and titanium screw. The lowest percent of metallic artifact was reduced by  $12.03\% \pm 1.02\%$  and  $13.01\% \pm 1.90\%$  in protocol 1 for both of stainless-steel and titanium screw as show in Table 11 and Table 12 respectively.

**Table 9.** The results of volume metallic artifact in stainless steel screw.

Imaging protocol	Volume of metal artifact 1 <sup>st</sup> (cm <sup>3</sup> )	Volume of metal artifact 2 <sup>nd</sup> (cm <sup>3</sup> )	Volume of metal artifact 3 <sup>rd</sup> (cm <sup>3</sup> )	Mean $\pm$ SD
Protocol 1	160.48	163.49	163.95	$162.64 \pm 1.88$
Protocol 2	158.55	159.95	156.40	$158.30 \pm 1.79$
Protocol 3	160.16	157.85	155.44	$157.82 \pm 2.36$
Protocol 4	126.73	127.47	125.09	$126.43 \pm 1.22$
Protocol 5	124.71	125.21	124.69	$124.87 \pm 0.29$
Protocol 6	123.69	123.98	121.12	$122.93 \pm 1.57$
Protocol 7	116.41	118.43	117.80	$117.55 \pm 1.03$
Protocol 8	113.07	115.38	116.02	$114.82 \pm 1.55$
Protocol 9	112.40	111.97	112.83	$112.40 \pm 0.43$
Protocol 10	184.66	183.83	186.17	$184.89 \pm 1.19$

**Table 10.** The results of volume of metallic artifact in titanium screw.

<b>Imaging protocol</b>	<b>Volume of metal artifact 1<sup>st</sup> (cm<sup>3</sup>)</b>	<b>Volume of metal artifact 2<sup>nd</sup> (cm<sup>3</sup>)</b>	<b>Volume of metal artifact 3<sup>rd</sup> (cm<sup>3</sup>)</b>	<b>Mean <math>\pm</math> SD</b>
Protocol 1	34.87	33.71	32.82	33.80 $\pm$ 1.03
Protocol 2	33.03	32.58	32.07	32.56 $\pm$ 0.48
Protocol 3	33.70	32.94	34.74	33.79 $\pm$ 0.90
Protocol 4	14.16	13.01	12.99	13.39 $\pm$ 0.67
Protocol 5	13.06	13.72	14.52	13.77 $\pm$ 0.73
Protocol 6	12.18	13.01	13.02	12.74 $\pm$ 0.48
Protocol 7	11.68	10.84	10.15	10.89 $\pm$ 0.77
Protocol 8	11.74	11.84	10.68	11.42 $\pm$ 0.64
Protocol 9	9.89	10.83	11.28	10.67 $\pm$ 0.71
Protocol 10	39.92	38.01	38.64	38.86 $\pm$ 0.97

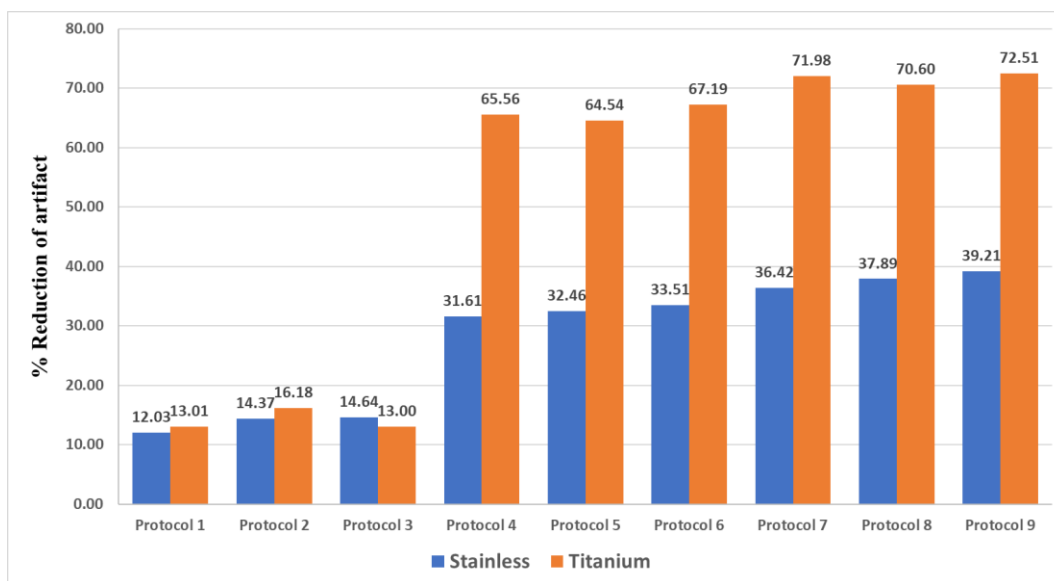
**Table 11.** The results of percent of metallic artifact reduction comparing SPACE sequences (protocol 1-9) to TSE sequences (protocol 10) in stainless steel screw.

<b>Imaging protocol</b>	<b>Metallic artifact reduction (%)</b>	<b>Ranking score</b>
Protocol 1	12.03 $\pm$ 1.02	2
Protocol 2	14.37 $\pm$ 1.51	3
Protocol 3	14.64 $\pm$ 1.68	4
Protocol 4	31.61 $\pm$ 1.10	5
Protocol 5	32.46 $\pm$ 0.57	6
Protocol 6	33.51 $\pm$ 1.26	7
Protocol 7	36.42 $\pm$ 0.74	8
Protocol 8	37.89 $\pm$ 0.79	9
Protocol 9	39.21 $\pm$ 0.16	10
Protocol 10	-	1

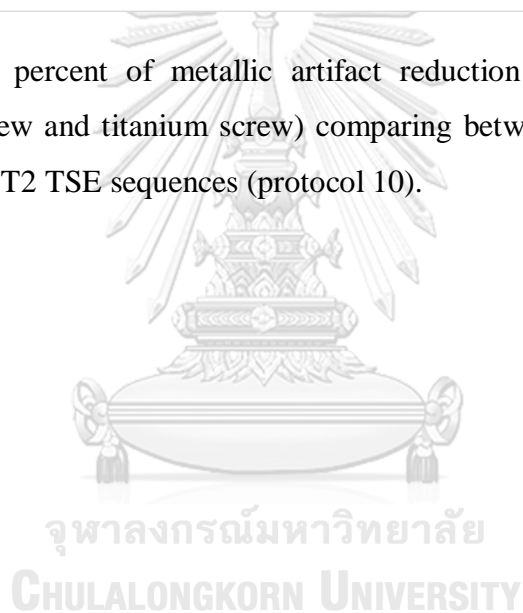
**Table 12.** The results of percent of metallic artifact reduction comparing SPACE sequences (protocol 1-9) to TSE sequences (protocol 10) titanium screw.

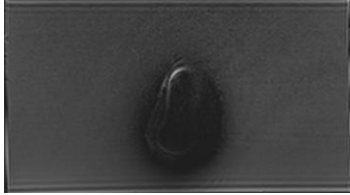
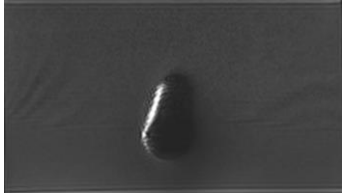
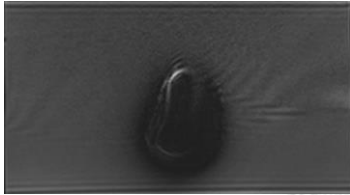
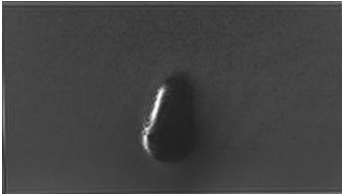
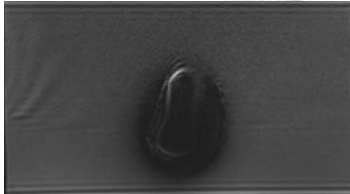
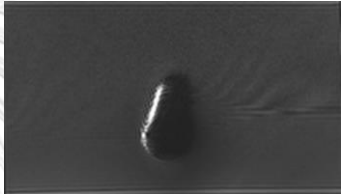
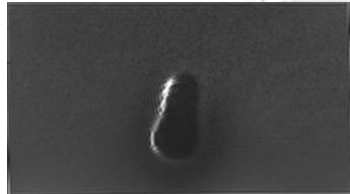
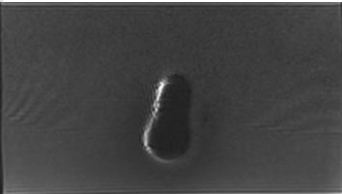
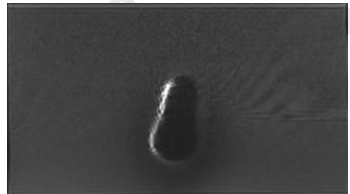
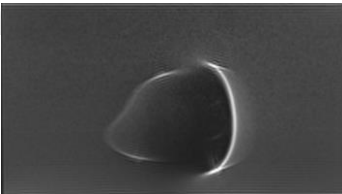
Imaging protocol	Metallic artifact reduction	Ranking score
Protocol 1	13.01±1.90	2
Protocol 2	16.18±1.65	4
Protocol 3	13.00±2.76	3
Protocol 4	65.56±0.94	6
Protocol 5	64.54±2.49	5
Protocol 6	67.19±2.01	7
Protocol 7	71.98±1.56	9
Protocol 8	70.60±1.75	8
Protocol 9	72.51±2.37	10
Protocol 10	-	1

The titanium screw produced much less artifact than the stainless-steel screw for both TSE and SPACE sequence as illustrated in Figure 24. The images with 10 protocols were assessed by ranking score (1-10 points) to determine the appropriate parameters in terms of volume of metallic artifact, signal-to-noise ratio (SNR) and specific absorption rate (SAR) as shown in Figure 27. The metal artifact with the use of SPACE was markedly reduced compared with the TSE sequence, for both of stainless steel and titanium screw as shown in Figure 25 and 26. All protocols evaluated in this study have the same trend in metal artifact reduction for different metal material.

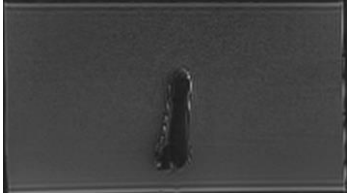
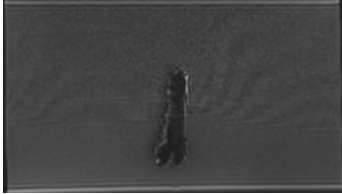
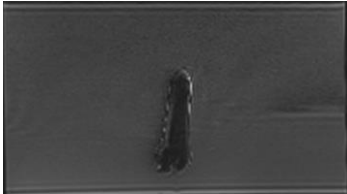
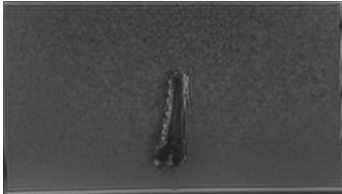
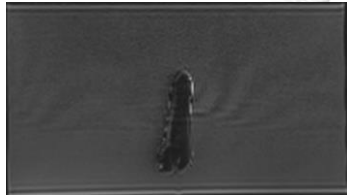
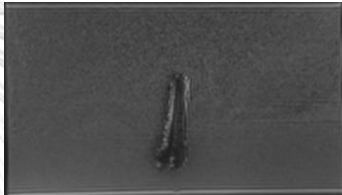
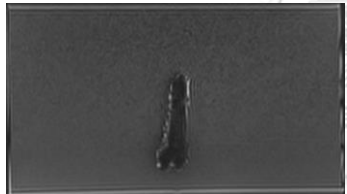
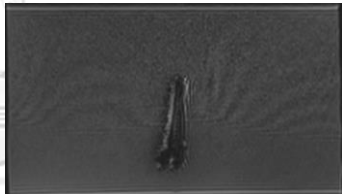
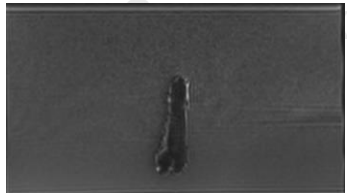
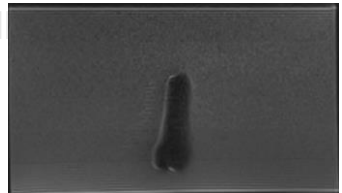


**Figure 24:** The percent of metallic artifact reduction for both metal implants (stainless steel screw and titanium screw) comparing between T2 SPACE sequences (protocol 1-9) and T2 TSE sequences (protocol 10).



<b>Protocol 1</b>  $162.64 \pm 1.88 \text{ cm}^3$	<b>Protocol 6</b>  $122.93 \pm 1.57 \text{ cm}^3$
<b>Protocol 2</b>  $158.30 \pm 1.79 \text{ cm}^3$	<b>Protocol 7</b>  $117.55 \pm 1.03 \text{ cm}^3$
<b>Protocol 3</b>  $157.82 \pm 2.36 \text{ cm}^3$	<b>Protocol 8</b>  $114.82 \pm 1.55 \text{ cm}^3$
<b>Protocol 4</b>  $126.43 \pm 1.22 \text{ cm}^3$	<b>Protocol 9</b>  $112.40 \pm 0.43 \text{ cm}^3$
<b>Protocol 5</b>  $124.87 \pm 0.29 \text{ cm}^3$	<b>Protocol 10</b>  $184.89 \pm 1.19 \text{ cm}^3$

**Figure 25:** The images of the metallic artifacts acquired from cylinder plastic phantom filled with solution containing one stainless steel screw evaluated at 1.5 Tesla with T2 weighted TSE sequence (protocol 10), SPACE sequence (protocol 1-9).

<b>Protocol 1</b>  $33.80 \pm 1.03 \text{ cm}^3$	<b>Protocol 6</b>  $12.74 \pm 0.48 \text{ cm}^3$
<b>Protocol 2</b>  $32.56 \pm 0.48 \text{ cm}^3$	<b>Protocol 7</b>  $10.89 \pm 0.77 \text{ cm}^3$
<b>Protocol 3</b>  $33.79 \pm 0.90 \text{ cm}^3$	<b>Protocol 8</b>  $11.42 \pm 0.64 \text{ cm}^3$
<b>Protocol 4</b>  $13.39 \pm 0.67 \text{ cm}^3$	<b>Protocol 9</b>  $10.67 \pm 0.71 \text{ cm}^3$
<b>Protocol 5</b>  $13.77 \pm 0.73 \text{ cm}^3$	<b>Protocol 10</b>  $38.86 \pm 0.97 \text{ cm}^3$

**Figure 26:** The images of the metallic artifacts acquired from cylinder plastic phantom filled with solution containing one titanium screw evaluated at 1.5 Tesla with T2 weighted TSE sequence (protocol 10), SPACE sequence (protocol 1-9).

#### 4.5 Image quality evaluation

Signal-to-noise ratio (SNR) was measured in order to evaluate image quality in each protocol. The highest SNRs of  $23.03 \pm 0.64$  and  $25.43 \pm 0.22$  were obtained in protocol 6 for both stainless-steel and titanium screw. The lowest SNRs of  $18.19 \pm 1.49$  and  $18.53 \pm 0.22$  were found in protocol 7 for both of stainless-steel and titanium screw as shown in Table 13 and 14.

**Table 13.** The results of signal-to-noise ratio (SNR) in stainless steel.

Imaging protocol	SNR 1 <sup>st</sup>	SNR 2 <sup>nd</sup>	SNR 3 <sup>rd</sup>	Mean $\pm$ SD	Ranking score
Protocol 1	21.42	19.22	20.49	$20.38 \pm 1.10$	5
Protocol 2	23.55	20.93	21.54	$22.01 \pm 1.37$	6
Protocol 3	23.59	20.97	22.36	$22.31 \pm 1.31$	8
Protocol 4	23.70	21.10	21.84	$22.21 \pm 1.34$	7
Protocol 5	24.32	21.92	22.80	$23.01 \pm 1.22$	9
Protocol 6	23.37	22.29	23.43	$23.03 \pm 0.64$	10
Protocol 7	19.76	16.80	18.03	$18.19 \pm 1.49$	1
Protocol 8	20.34	18.04	19.79	$19.39 \pm 1.20$	3
Protocol 9	21.15	16.54	16.98	$18.22 \pm 2.54$	2
Protocol 10	19.44	18.59	20.20	$19.41 \pm 0.81$	4

**Table 14.** The results of signal-to-noise ratio (SNR) in titanium screw.

Imaging protocol	SNR 1 <sup>st</sup>	SNR 2 <sup>nd</sup>	SNR 3 <sup>rd</sup>	Mean $\pm$ SD	Ranking score
Protocol 1	21.41	20.59	21.10	$21.03 \pm 0.41$	5
Protocol 2	23.95	23.66	24.07	$23.89 \pm 0.21$	7
Protocol 3	23.80	22.66	23.07	$23.18 \pm 0.58$	6
Protocol 4	24.01	23.68	24.58	$24.09 \pm 0.46$	8
Protocol 5	24.48	25.67	25.51	$25.22 \pm 0.65$	9
Protocol 6	25.31	25.69	25.30	$25.4 \pm 0.22$	10
Protocol 7	18.72	18.29	18.59	$18.53 \pm 0.22$	1
Protocol 8	20.20	20.02	20.43	$20.22 \pm 0.20$	4
Protocol 9	19.92	20.58	20.05	$20.18 \pm 0.35$	3
Protocol 10	18.59	19.44	19.45	$19.16 \pm 0.49$	2

#### 4.6 The Specific Absorption Rate (SAR)

In MRI safety, the concern for a rise in tissue temperature is greater in patient with implanted devices. The Specific Absorption Rate (SAR) was recorded in each scanning protocol in order to achieve the patient safety concern. The highest SARs of  $1.11\pm0.04$  and  $1.20\pm0.0012$  W/kg were obtained in protocol 9 for both stainless-steel and titanium screw. The lowest SARs of  $0.31\pm0.01$  and  $0.33\pm0.0012$  W/kg were found in protocol 1 for both of stainless-steel and titanium screw as shown in Table 15 and 16.

**Table 15.** The results of Specific Absorption Rate (SAR) in stainless steel.

Imaging protocol	SAR (W/kg) 1 <sup>st</sup>	SAR (W/kg) 2 <sup>nd</sup>	SAR (W/kg) 3 <sup>rd</sup>	Mean $\pm$ SD	Ranking score
Protocol 1	0.30	0.30	0.32	$0.31\pm0.01$	10
Protocol 2	0.64	0.66	0.69	$0.66\pm0.02$	7
Protocol 3	0.92	0.94	0.98	$0.95\pm0.03$	3
Protocol 4	0.33	0.33	0.35	$0.34\pm0.01$	9
Protocol 5	0.71	0.73	0.76	$0.73\pm0.03$	5
Protocol 6	1.02	1.04	1.09	$1.05\pm0.04$	2
Protocol 7	0.35	0.35	0.37	$0.36\pm0.01$	8
Protocol 8	0.76	0.77	0.81	$0.78\pm0.03$	4
Protocol 9	1.08	1.11	1.16	$1.11\pm0.04$	1
Protocol 10	0.60	0.72	0.76	$0.69\pm0.08$	6

**Table 16.** The results of Specific Absorption Rate (SAR) in titanium.

Imaging protocol	SAR (W/kg) 1 <sup>st</sup>	SAR (W/kg) 2 <sup>nd</sup>	SAR (W/kg) 3 <sup>rd</sup>	Mean $\pm$ SD	Ranking score
Protocol 1	0.33	0.33	0.33	$0.33\pm0.0012$	10
Protocol 2	0.72	0.71	0.71	$0.71\pm0.0006$	7
Protocol 3	1.02	1.02	1.02	$1.02\pm0.0012$	3
Protocol 4	0.36	0.36	0.36	$0.36\pm0.0006$	9
Protocol 5	0.79	0.79	0.79	$0.79\pm0.0012$	5
Protocol 6	1.13	1.13	1.13	$1.13\pm0.0006$	2
Protocol 7	0.39	0.38	0.38	$0.38\pm0.0006$	8
Protocol 8	0.84	0.84	0.84	$0.84\pm0.0006$	4
Protocol 9	1.20	1.20	1.20	$1.20\pm0.0012$	1
Protocol 10	0.79	0.78	0.78	$0.78\pm0.0006$	6



#### 4.7 Appropriate parameter selection

The images with 10 protocols were assessed by ranking score in terms of volume of metallic artifact, signal-to-noise ratio (SNR) and specific absorption rate (SAR). The highest score ranking of 21 and 23 were obtained in protocol 4 for both stainless-steel and titanium screw. The lowest score ranking of 11 and 9 were obtained in protocol 10 for both of stainless-steel and titanium screw as shown in Table 17 and 18.

**Table 17.** Ranking score of volume of metallic artifact, SNR and SAR in stainless steel.

Imaging protocol	Volume of metal artifact	SNR	SAR	Total score
Protocol 1	2	5	10	17
Protocol 2	3	6	7	16
Protocol 3	4	8	3	15
Protocol 4	5	7	9	21
Protocol 5	6	9	5	20
Protocol 6	7	10	2	19
Protocol 7	8	1	8	17
Protocol 8	9	3	4	16
Protocol 9	10	2	1	13
Protocol 10	1	4	6	11

**Table 18.** Ranking score of volume of metallic artifact, SNR and SAR in titanium.

Imaging protocol	Volume of metal artifact	SNR	SAR	Total score
Protocol 1	2	5	10	17
Protocol 2	4	7	7	18
Protocol 3	3	6	3	12
Protocol 4	6	8	9	23
Protocol 5	5	9	5	19
Protocol 6	7	10	2	19
Protocol 7	9	1	8	18
Protocol 8	8	4	4	16
Protocol 9	10	3	1	14
Protocol 10	1	2	6	9

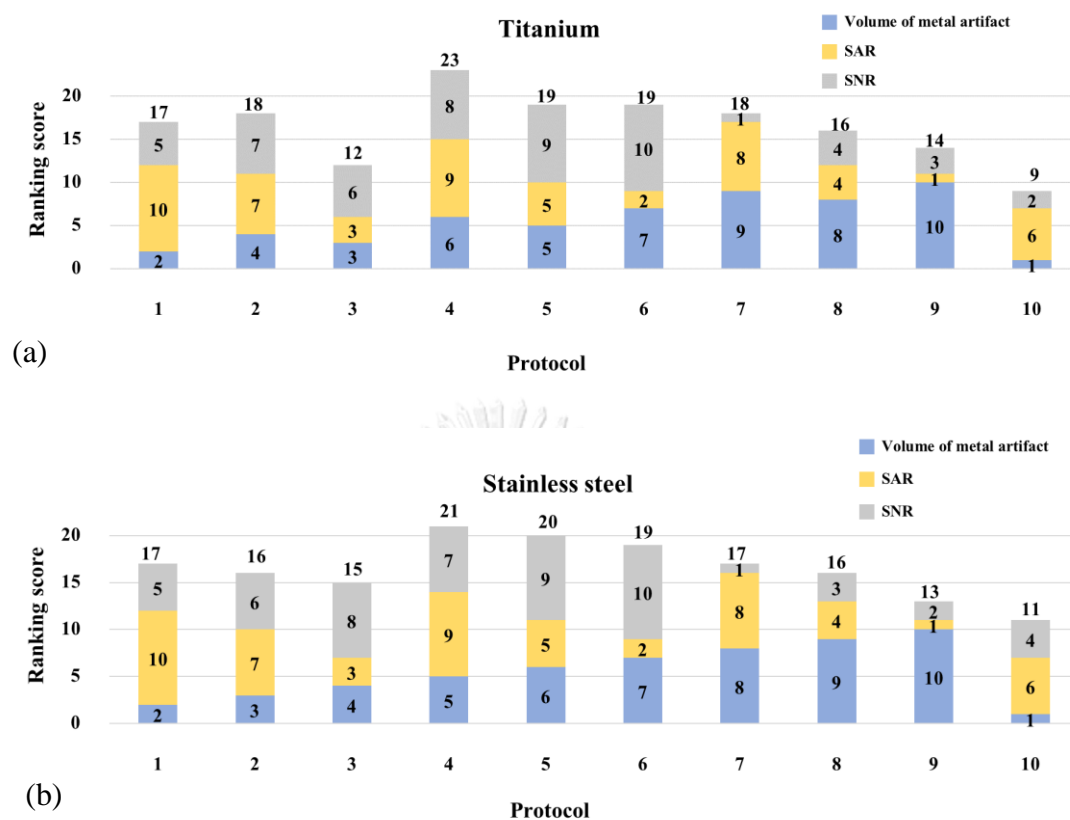


**Figure 27:** The ranking score of 10 protocols (a) titanium and (b) stainless steel.

## CHAPTER V

### DISCUSSION AND CONCLUSIONS

#### 5.1 Discussion

Presently, the various pulse sequences were developed for addressing the metallic artifact in MRI lumbar spine. There are many parameters affecting the MR image quality such as repetition time (TR), echo time (TE), flip angle, bandwidth, slice thickness, number of excitations, field of view (FOV), matrix size, etc. However, most of the routine protocols using for the lumbar spine examination embedded with prosthesis are not suitable for susceptibility artifact reduction. In this study, we have investigated the appropriate parameters for metallic artifact reduction using the latest pulse sequence provided by Siemens Medical System namely T2 3D-SPACE in MRI lumbar spine and compared with the conventional pulse sequence, turbo spin echo (TSE). According to the results in previous studies, in this study we emphasized to adjust the flip angle and receiver bandwidth in order to obtain the appropriate parameters based on phantom study.

In theoretical, the volume of susceptibility artifact is directly proportional to the strength of the frequency encoding gradient (GFE), which is itself defined by the following formula:

$$GFE = 2\pi BW/\gamma\Delta x \quad (5.1)$$

The gyromagnetic ratio ( $\gamma$ ) is fixed for a given field strength, but both of the receiver bandwidth and the voxel size ( $\Delta x$ ) can influence the magnitude of the frequency encoding gradient. In this study, we fixed  $\Delta x$  and increased bandwidth instead in order to increase the GFE. The results of the present study indicated that increasing receiver bandwidth can be consequently reduced the susceptibility artifact. Most of the achievable metal artifact reductions around 70% were found with receiver bandwidth of 723 Hz/pixel. In all protocols, increasing the receiver bandwidth resulting in a substantial reduction of SNR due to the noises are also increased, but still produces acceptable images quality for diagnostic purposes based on our visual observation. This should be considered as the primarily parameters for metal artifact

reduction without changing the matrix size. By decreasing the voxel size to increase the GFE, as a result, the resolution of the phase-encoding direction of the matrix increases proportion to the acquisition time. Increasing the matrix in phase-encoding direction will prolong the scanning time. However, according to the previous study from Aboelmagd et al (17), they reported that the susceptibility artifact can be reduced in the frequency-encoding direction by increasing the receiver bandwidth, although this effect has the saturation at about 400 Hz/pixel on MRI 1.5 T system.

As expectation, titanium screw produces much less artifact and distortion than stainless steel screw since the titanium screw is a paramagnetic material that has a positive magnetic moment and small attractive effect on the local field. In contrast, the stainless-steel screw is a ferromagnetic material as it is a positive magnetic moment and stronger attractive magnetic susceptibility. Therefore, the SPACE sequence can dramatically reduce the volume of the artifact for the titanium screw approximately 13-70%, and for the stainless-steel screw by 12-40% compared to TSE acquisitions.

In MRI safety, the concern for a rise in tissue temperature is greater in patient with implanted devices that may have much higher risk from exposure to MRI radiofrequency pulses and must be evaluated. Since spin-echo MRI techniques use large radiofrequency pulses for the flip angle  $90^\circ$  and  $180^\circ$  manipulation of tissue magnetization, TSE applies large radiofrequency pulses very rapidly accordingly as shown in Figure 28. As a result, The TSE delivers more radiofrequency power resulting in higher SAR.

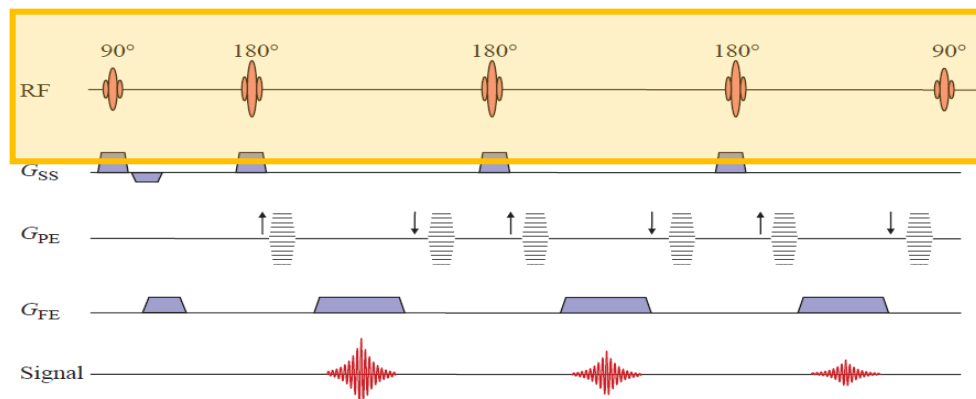


**Figure 28:** Turbo spin-echo sequence with an echo train length (turbo factor) of 3.

For SPACE pulse sequence, it uses low flip angle refocusing train, starting the pulse train with higher amplitude pulses and slowly decrease automatically approach to a constant (“asymptotic”) value, enables acquisition of images with SNR values close to those acquired with  $180^\circ$  refocusing pulses (13) as shown in Figure 29. For stainless steel at flip angle  $150^\circ$  and bandwidth 256 Hz/pixel, SPACE protocol provided slightly lower SAR (0.66 W/kg) compared to TSE (0.69 W/kg). For titanium at the same flip angle and bandwidth, SPACE protocol also provided lower SAR (0.71 W/kg) compared to TSE (0.78 W/kg). However, at the other bandwidths and same flip angle, SPACE provided SAR higher than conventional sequences due to higher RF pulse bandwidth will increase the SAR accordingly.

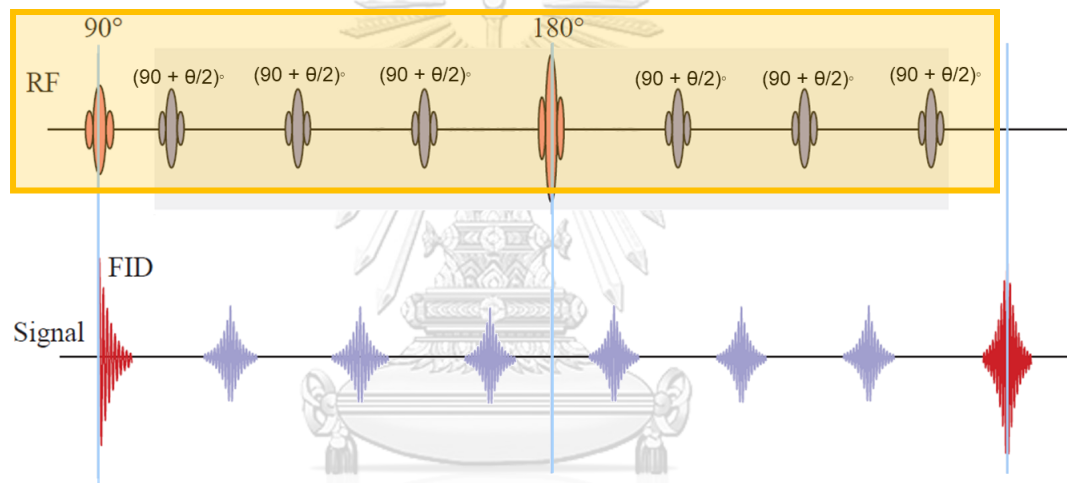


**Figure 29:** SPACE pulse sequence.

In previous study by Neil M. Kumar et al (18), they used sensing slice encoding for metal artifact correction (SEMAC) and TSE pulse sequences by varying long echo train length (ETL) ranging from 3 to 23 and receiver bandwidth from 100 to 750 Hz/pixel. They found that high receiver bandwidth was the most effective parameter for reduction of arthroplasty implant-induced metal artifact on MRI scans, whereas echo train length cause degradation of image quality around the implant with larger appearing total metal artifacts. In our study, we used TSE and SPACE sequences by varying the flip angle of  $100^\circ$ ,  $150^\circ$ ,  $180^\circ$  and receiver bandwidth of 296, 501 and 723 Hz/pixel. According to Neil M. Kumar et al (18), higher receiver bandwidth can reduce metallic artifact. However, increasing the receiver bandwidth, the noises was increased resulting reduction of image quality. According to Tao Ai et

al (3), they used 3D TSE (bandwidth 751 Hz/pixel) and MSVAT-SPACE (bandwidth 930 Hz/pixel). They found that the MSVAT-SPACE showed significant metal artifact reduction compared with 3D TSE. However, the blurring in MSVAT-SPACE is more evident than on the 3D TSE sequence.

The acquisitions time in SPACE was lengthy around 12:05 min compared with conventional sequences (5:31 min) at 1.5 T. However, the SPACE provides the reconstructed image in 3-planes simultaneously (transverse, coronal, sagittal), whereas the TSE provides reconstructed image in each plane according to the routine MRI pulse sequences protocol at KCMH. Totally, the overall scan time of SPACE is nearby the TSE. Scan time can be considerably reduced by utilizing dedicated acquisition techniques such as parallel imaging, partial Fourier sampling and longer echo train length.

There were a few limitations in this study such as the method of volumetric measurement to quantify metal artifacts which is based on the signal change caused by the metal implants. The results of measurement also influenced by the chosen threshold level setting as the GE workstation software accepted only the integer number for the input parameter. The accuracy in the total volume measurement of each artifact could be affected. Basically, the methodology to determine the volume of metallic artifact accurately plays an important role for metallic artifact reduction evaluation. In this study, the equation used to evaluate the normal background range was calculated by using the mean signal intensity $\pm$ 3SD following Tao Ai et al (3), to determine the area under normal distribution histogram of the image without metallic artifact. As shown in Figure 30, at the area under the curve of mean $\pm$ 3SD, 99.7% of the data will be used to calculate the range of normal signal intensity representing the lower and upper threshold levels of the normal background. According to the experimental results for verifying this equation to calculate the volume of solution in phantom, it was found that the calculated volume was close to the known volume of solution filled in the phantom as described in CHAPTER 4. Therefore, it was ensured that using such equation as in the literature is appropriated for determining the artifact volume accurately in MRI image.

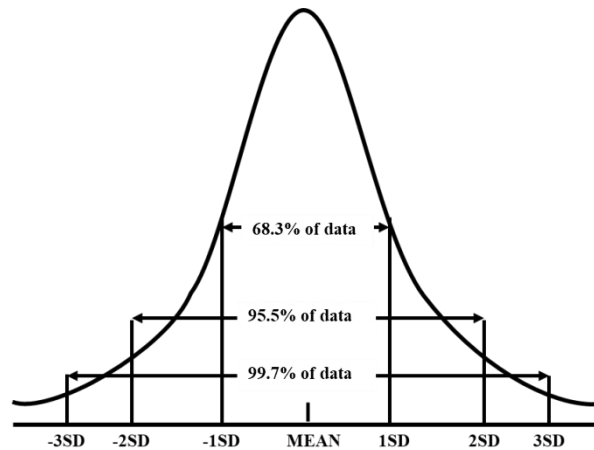


**Figure 30:** Areas under the normal curve that lie between 1, 2 and 3 standard deviations on each side of the mean.

Another limitation was the image quality between conventional 2D-TSE and 3D-SPACE images could not directly comparable due to the difference in 2D and 3D acquisition techniques such as slice thickness, interslice gap, and the parallel imaging. Consequently, in order to reduce the bias in acquiring the phantom using 3D SPACE protocol, the parallel imaging was removed from this study. The appropriate parameters in this study were obtained based on the investigation in cylindrical phantom filled with biological conductivity solution. Therefore, these parameters should be further applied in patients for testing the performance of metallic artifact reduction protocols using 3D SPACE in clinical study in future.

In clinical, the use of 3D SPACE imaging for the spine has been extremely useful with high-resolution imaging of pathologic abnormalities and multi-planar reformatting capabilities. The resolution afforded by SPACE allows better evaluation of nerve roots, small facet joint cysts, bone spurs, and disk fragments that cause nerve root impingement at all lumbar levels as some of which are not clearly detected on the 2D TSE T2-weighted images (16).

Even though the main purpose of our study was to investigate the appropriate 3D T2 SPACE parameters for reducing the metallic artifact in MR lumbar spine image, the obtained image quality in terms of SNR was also considered as mentioned previously. Increasing the receiver bandwidth, however, causes degradation of image quality. Additionally, the risk of tissue heating should be concerned in MRI

examination especially with patients having the metallic implant, and pediatric patients. Consequently, we have also tried to balance the acceptable image quality level and tissue heating by varying the flip angle for SPACE sequence in order to observe which parameters can provide the SAR value as low as possible. The SAR refers to the amount of energy absorbed by the patient during an MRI scan sequence. A higher SAR relatively makes more tissue heating. According to the IEC regulation, limitations apply to the SAR level allow 2 W/kg for whole-body in normal mode, and 4 W/kg in first level-controlled mode, which requires medical supervision to the patient (14). As a result, the appropriate parameters in this thesis was not only based on the capability of the pulse sequence that enables to reduce the artifact volume and provide adequate image quality, but also considered the SAR level for the patient safety concern as the best practice guideline (14).

The issue that might be the weakness of this study was the lack of weighting values for scoring in each topic for selecting the optimization protocol. Even the slightly difference of metallic artifact volume, SNR, and SAR values, this would make the large difference of scoring according to the sorting criteria in this study. This was one of the factors affecting for the optimized parameter selection. If possible, therefore, the weighted value is suggested from this study for the scoring criteria in determining the appropriate parameters for the new MRI pulse sequence for the future study.

## 5.2 Conclusions

Using the SPACE pulse sequence, the artifact volume can be effectively reduced by increasing the receiver bandwidth. The metal artifacts were reduced highest at protocol 9 by 39.21% for stainless steel and 72.55% for titanium. The highest-ranking scores were protocol 4 and 5 by considering of SAR and SNR. The appropriate parameters for metallic artifact reduction using 3D SPACE according to selected protocols were the bandwidth 501 Hz/pixel, flip angle 100° and 150° in both of stainless steel and titanium respectively.





จุฬาลงกรณ์มหาวิทยาลัย  
**CHULALONGKORN UNIVERSITY**

## REFERENCES

1. Hargreaves BA, Woters PW, Pauly KB, Pauly JM, Koch KM, Gold GE. Metal-Induced Artifacts in MRI. *American Journal of Roentgenology*. 2011;197(3):547-55.
2. Olsen RV, Munk PL, Lee MJ, Janzen DL, MacKay AL, Xiang Q-S, et al. Metal artifact reduction sequence: early clinical applications. 2000;20(3):699-712.
3. Ai T, Padua A, Goerner F, Nittka M, Gugala Z, Jadhav S, et al. SEMAC-VAT and MSVAT-SPACE Sequence Strategies for Metal Artifact Reduction in 1.5T Magnetic Resonance Imaging. *Investigative Radiology*. 2012;47(5):267-76.
4. Sprawls P. *Physical principles of medical imaging*: Aspen Publishers; 1987.
5. Ariyanayagam T, Malcolm PN, Toms AP, editors. *Advances in metal artifact reduction techniques for periprosthetic soft tissue imaging*. *Seminars in musculoskeletal radiology*; 2015: Thieme Medical Publishers.
6. Lichy M, Horger W, Mugler J, Menzel MI, Kiefer B, Schlemmer H. T2-Weighted 3D MR Imaging of the Torso—First Clinical Experiences with SPACE.
7. Haacke EM, Brown RW, Thompson MR, Venkatesan R. *Magnetic resonance imaging: physical principles and sequence design*: Wiley-Liss New York; 1999.
8. Brown RW, Haacke EM, Cheng Y-CN, Thompson MR, Venkatesan R. *Magnetic resonance imaging: physical principles and sequence design*: John Wiley & Sons; 2014.
9. Rangwala NA. *Reduction of Artifacts Arising From Non-Ideal Gradients in Fast Magnetic Resonance Imaging* 2012.
10. Lauterbur PC. Image formation by induced local interactions: examples employing nuclear magnetic resonance. 1973.
11. den Harder J. *Metal implant artifact reduction in magnetic resonance imaging*: Citeseer; 2015.
12. Koch KM, King KF, Carl M, Hargreaves BA. Imaging near metal: the impact of extreme static local field gradients on frequency encoding processes. *Magnetic resonance in medicine*. 2014;71(6):2024-34.
13. Scott K, Schmeets S. SPACE: an innovative solution to rapid low SAR T2-weighted contrast in 3D spin echo imaging. *Magnetom Flash*. 2005:92-5.
14. CODE P, PRIX C. *Medical electrical equipment—Part 2-33: Particular requirements for the safety of magnetic resonance equipment for medical diagnosis Appareils électromédicaux—Partie 2-33: Règles particulières de sécurité relatives aux appareils à résonance*. 2002.
15. Filli L, Jud L, Luechinger R, Nanz D, Andreisek G, Runge VM, et al. Material-Dependent Implant Artifact Reduction Using SEMAC-VAT and MAVRIC: A Prospective MRI Phantom Study. *Investigative Radiology*. 2017;52(6):381-7.
16. Sayah A, Jay AK, Toaff JS, Makariou EV, Berkowitz F. Effectiveness of a Rapid Lumbar Spine MRI Protocol Using 3D T2-Weighted SPACE Imaging Versus a Standard Protocol for Evaluation of Degenerative Changes of the Lumbar Spine. *American Journal of Roentgenology*. 2016;207(3):614-20.
17. Aboelmagd SM, Malcolm PN, Toms APJRI. *Magnetic resonance imaging of metal artifact reduction sequences in the assessment of metal-on-metal hip prostheses*. 2014;7:65.
18. Kumar NM, de Cesar Netto C, Schon LC, Fritz JJr. *Metal artifact reduction magnetic resonance imaging around arthroplasty implants: the negative effect of long*

echo trains on the implant-related artifact. 2017;52(5):310-6.



### Appendix A: Case record form

**Table 19.** Mean signal intensities (Mean $\pm$ SD) in each protocol of the phantom filled with 3.3 g/L, NiCl<sub>2</sub>-6H<sub>2</sub>O and 2.4 g/L NaCl solution.

Imaging protocol	Mean signal intensity	Standard deviation	Lower threshold	Upper threshold	Volume
Protocol 1					
Protocol 2					
Protocol 3					
Protocol 4					
Protocol 5					
Protocol 6					
Protocol 7					
Protocol 8					
Protocol 9					
Protocol 10					

**Table 20.** The volume metallic artifact in stainless steel screw.

Imaging protocol	Volume of metal artifact 1st (cm <sup>3</sup> )	Volume of metal artifact 2nd (cm <sup>3</sup> )	Volume of metal artifact 3rd (cm <sup>3</sup> )	Mean $\pm$ SD
Protocol 1				
Protocol 2				
Protocol 3				
Protocol 4				
Protocol 5				
Protocol 6				
Protocol 7				
Protocol 8				
Protocol 9				
Protocol 10				

**Table 21.** The volume metallic artifact in titanium.

<b>Imaging protocol</b>	<b>Volume of metal artifact 1st (cm3)</b>	<b>Volume of metal artifact 2nd (cm3)</b>	<b>Volume of metal artifact 3rd (cm3)</b>	<b>Mean <math>\pm</math> SD</b>
Protocol 1				
Protocol 2				
Protocol 3				
Protocol 4				
Protocol 5				
Protocol 6				
Protocol 7				
Protocol 8				
Protocol 9				
Protocol 10				

## Appendix B: Quality control of MRI scanner

**Location:** MRI Room 2 at first floor of 14 floor Building

**Date:** 30 March 2018

**Equipment:**

MRI System Manufacturer: Siemens Healthcare

Model: MAGNETOM, Aera 1.5 Tesla

QC Phantom: ACR Phantom

Serial number: J11710

Quality of MRI system consists of

1. Geometric Accuracy
2. High contrast spatial resolution
3. Slice Thickness Accuracy
4. Slice position accuracy
5. Image intensity uniformity
6. Percent signal ghosting
7. Low contrast object Detectability
8. Image Artifact Evaluation
9. Magnet Visual Inspection

### Procedures the QC Phantom

Place the QC phantom on the head coil and level it. Turn “NOSE” side to tilt the top of phantom and turn “CHIN” side away from the gantry. Use the laser alignment light to position the phantom.

The MRI accreditation program requires the acquisition of a sagittal localizer and four axial series of image. The same set of eleven slice locations within the

phantom is required using the scanner's head coil. The scan parameters for the localizer and the first two axial series of imaged are fully prescribed by ACR in the scanning instructions as the ACR sequence or ACR image. The third and fourth series of axial image based on King Chulalongkorn Memorial Hospital is the spin echo T1 and T2 protocols and are referred to set the sequence or site images. To discuss the image data, it is convenient to introduce name for the different sets of image and numbering for the slice locations within the phantom.

The localizer is a 20 mm thick single slice spin echo acquisition through the center of phantom and is referred to simply as the localizer.

A sagittal locator sequence should be acquired with the acquisition parameters listed on the Site Scanning Data Form. The sagittal locator scan result in an image similar to Figure 31. If the pairs of 45° crossed wedges are not visible in the scan, the phantom must be repositioned and rescanned. A horizontal line used for slice prescription should be parallel to the low contrast disks located at the top.

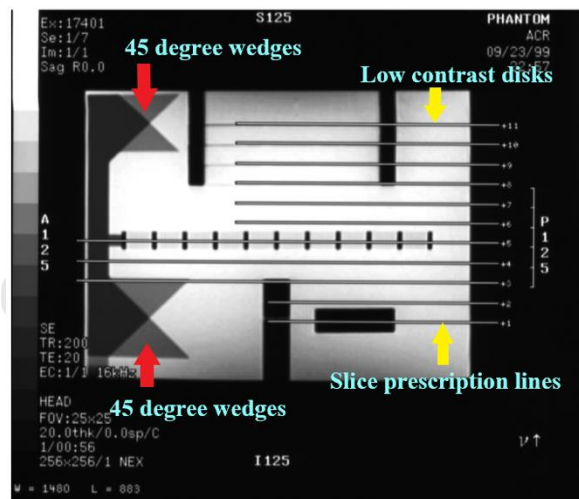


**Figure 31:** Sagittal localizer view of ACR MRI Phantom with slice locations for trans axial scans indicated.

The first axial series is a spin echo acquisition with ACR specified scan parameters that are typical of T1-weighted acquisitions. This series is called the ACR T1 series.

The second axial series is a double spin echo acquisitions with ACR specified scan parameters that are typical of proton density/T2-weighted acquisitions. When analyzing data from this acquisition, only the second-echo image is used. The set of second-echo image from this acquisition is called the ACR T2 series.

The third and fourth axial series are based on the scan parameters at King Chulalongkorn Memorial Hospital normally used its clinical protocols for axial head T1 and head T2 weighting. These series are called the clinical T1 and clinical T2.

**Table 22.** ACR pulse sequence acquisition parameters.

Series	Sequence	TR (msec)	TE (msec)	FOV (mm)	Thickness (mm)
Localization/Sagittal	SE	200	20	250	20
ACR T1	SE	500	20	250	5
ACR T2	SE	2000	20/80	255	5
Clinical Brain T1	SE	525	12	220	5
Clinical Brain T2	TSE	3989	100	250	6

**Table 23.** ACR pulse sequence acquisition parameters.

Series	Gap (mm)	NEX	Matrix	BW (kHz)	Scan time (min:sec)
Localization/Sagittal	N/A	1	256×256	290	0.30
ACR T1	5	1	256×265	110	2.18
ACR T2	5	1	256×256	89	8.36
Clinical Brain T1	0	1	256×256	110	3.10
Clinical Brain T2	1	1	255×255	89	4.06



## 1. Geometric Accuracy

**Purpose:** To assess the accuracy of the image lengths in the imaged subject. A failure means that dimensions in the images differ from the true dimensions substantially more than  $\pm 2$  mm.

### Methods

1. Display the localizer, measure the end-to-end length of the phantom as it appears in the localizer (line No.1).
2. Display slice 1 of the ACR T1 series. Measure the diameter of the phantom in 2 directions: top-to-bottom (line No.2) and left-to-right (line No.3).
3. Display slice 5 of the ACR T1 series. Measure the diameter of the phantom in 4 directions: top-to-bottom (line No.4), left-to-right (line No.5)

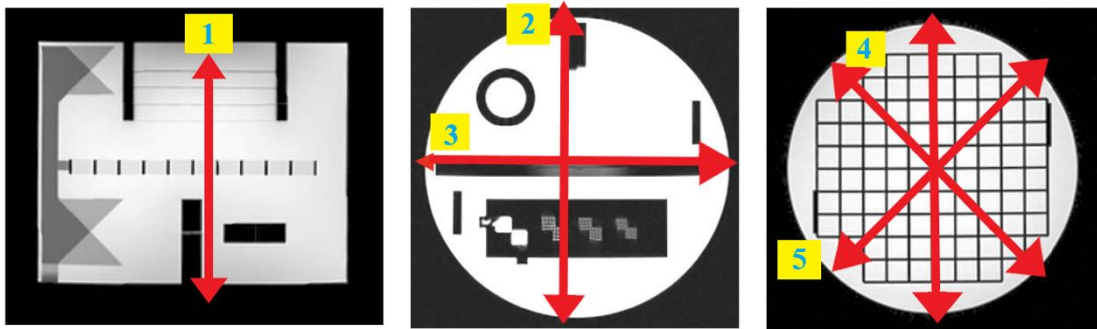


**Figure 32:** The end to end length and diameter measurement illustrated of the phantom.

**Table 24.** Geometric accuracy test results used ACR protocols.

Line No.	True value (mm)	Sagittal localizer		ACR T1		ACR T2 TE20		ACR T2 TE80	
		Meas. (mm)	Diff (mm)	Meas. (mm)	Diff (mm)	Meas. (mm)	Diff (mm)	Meas. (mm)	Diff (mm)
1	148	148.37	-0.37	-	-	-	-	-	-
2	190	-	-	192.41	-2.41	191.33	-1.33	191.94	-1.94
3	190	-	-	191.19	-1.19	190.11	-0.11	189.82	0.18
4	190	-	-	191.23	-1.23	190.92	-0.92	190.61	-0.61
5	190	-	-	191.18	-1.18	190.52	-0.52	189.76	0.24

**Table 25.** Geometric accuracy test results used routine protocols.

Line No.	True value (mm)	Sag locator		Clinical T1		Clinical T2	
		Meas. (mm)	Diff (mm)	Meas. (mm)	Diff (mm)	Meas. (mm)	Diff (mm)
1	148	147.7	-0.3	-	-	-	-
2	190	-	-	191.38	-1.38	191.66	-1.66
3	190	-	-	190.44	-0.44	189.84	0.16
4	190	-	-	190.83	-0.83	190.47	-0.47
5	190	-	-	190.54	-0.54	190.73	-0.73

**Recommended Action Criteria:** All measured dimension should be within  $\pm 2$  mm of their true values.

**Result:** PASSED

## 2. High contrast spatial resolution

**Purpose:** To assess the scanner's ability to resolve small objects when the contrast-to-noise ratio is sufficiently high.

### Methods

1. Display the slice 1.
2. Magnify the image by a factor of between 2 and 4, keeping the resolution insert visible in the display. This is illustrated in Figure 33.
3. Begin with the leftmost pair of hole arrays, which is the pair with the largest hole size, 1.1 mm.
4. Look at the rows of holes in the UL array, and adjust the display window and level to best show the holes as distinct from one another.
5. If all 4 holes in any single row are distinguishable from one another, score the image as resolved right- to-left at this particular hole size.

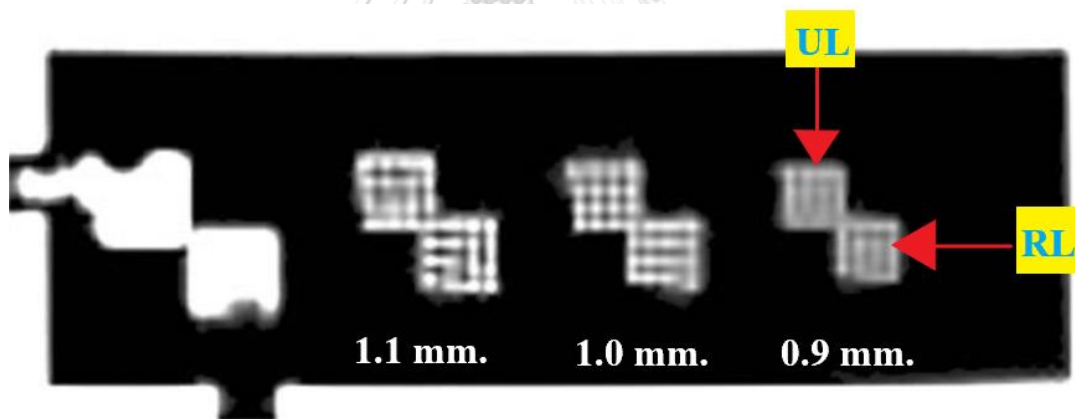


**Figure 33:** Magnified portion of slice 1 displayed appropriately for visually assessing high contrast resolution.

**Table 26.** Results of High Contrast Spatial Resolution test.

Series	Spatial Resolution(mm)		Result
	UL	RL	
ACR Axial T1	1.0	1.0	PASS
ACR Axial T2 TE 20	1.0	1.0	PASS
ACR Axial T2 TE 80	1.0	1.0	PASS
Clinical Axial T1	1.0	1.0	PASS
Clinical Axial T2	0.9	0.9	PASS

**Recommended Action Criteria:** the measured resolution should be 1.0 mm or smaller.

**Result:** PASSED



### 3. Slice Thickness Accuracy

**Purpose:** To assess the accuracy of a slice of specified thickness. The prescribed slice thickness is compared with the measured slice thickness.

#### Methods

For each ACR series, the length of the signal ramps in slice 1 is measured according to the following procedure:

1. Display slice 1 and magnify the image by a factor of 2 to 4. Adjust the display level so that the signal ramps are well visualized. The ramp signal is much lower than surrounding water.
2. Place a rectangular ROI at the middle of each signal ramp as shown in Figure 34. Note the mean signal values for each of these 2 ROIs then average those 2 values together. The result is a number approximating the mean signal in the middle of the ramps.

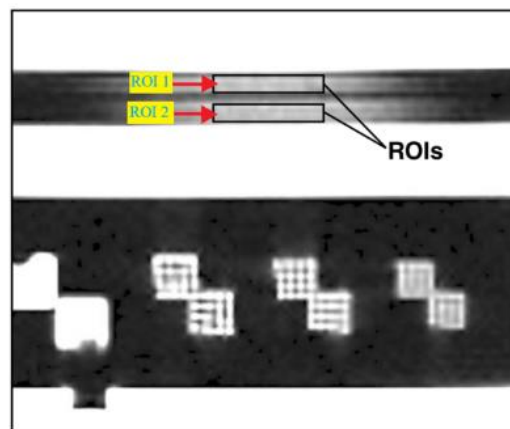


**Figure 34:** ROIs placed for measuring average signal in the ramps.

3. Display level to half of the average ramp signal calculated. Use the on-screen length measurement tool of the display station to measure the lengths of the top and bottom ramps. Record these lengths.

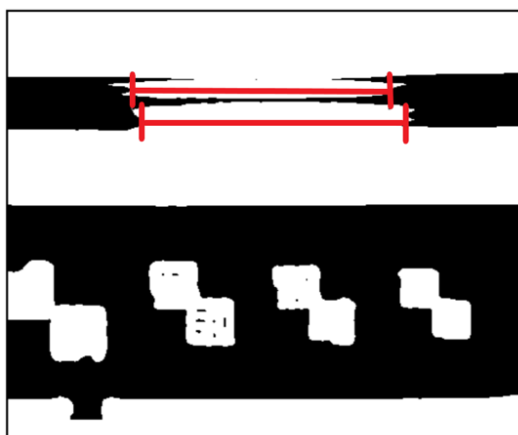


**Figure 35:** Magnified region of slice 1 showing slice thickness signal ramps.

4. The slice thickness is calculated using the following formula

$$\text{Slice thickness} = 0.2 \times (\text{top} \times \text{bottom}) / (\text{top} + \text{bottom}) \quad (\text{B.1})$$

**Table 27.** Slice thickness accuracy test result.

Series	Slice Thickness Setting (mm)	Slice Thickness Measurement (mm)	Difference (mm)	Result
ACR T1	5	4.74	0.26	Pass
ACR T2 TE 20	5	4.68	0.32	Pass
ACR T2 TE 80	5	4.65	0.35	Pass
Clinical T1	5	5.56	-0.56	Pass
Clinical T2	5	5.59	-0.59	Pass

**Recommended Action Criteria:** the measured thickness should be  $5.0 \pm 0.7$  mm

**Result:** PASSED

#### 4. Slice position accuracy

**Purpose:** To assesses the accuracy with which slices can be prescribed at specific locations utilizing the localizer image for positional reference.

##### Methods

Slice position accuracy test the differences between the prescribed and actual positions of slices 1 and 11 are measured. These measurements are made for the ACR T1 and T1 series. The slices 1 and 11 are prescribed so as to be aligned with the vertices of the crossed 45° wedges at the inferior and superior ends of the phantom respectively.

On slices 1 and 11 the crossed wedges appear as a pair of adjacent, dark, vertical bars at the top (anterior side) of the phantom.

For both slice 1 and slice 11, if the slice is exactly aligned with the vertex of the crossed wedges, then the wedges will appear as dark bars of equal length on the image. By design of the wedges, if the slice is displaced superiorly with respect to the vertex, the bar on the observer's right (anatomical left) will be longer. If the slice is displaced inferiorly with respect to the vertex, the bar on the left will be longer.

Measurements are made for slices 1 and 1 of the ACR T1 and ACR T2 series. Use the following procedure for each image:

1. Display the slice. Magnify the image by a factor of 2 to 4, keeping the vertical bars of the crossed wedges within the displayed portion of the magnified image.
2. Adjust the display window so the ends of the vertical bars are well defined and use the on-screen length measurement tool to measure the difference in length between the left and right bars. The length to measure is indicated by the arrows in Figure 36.

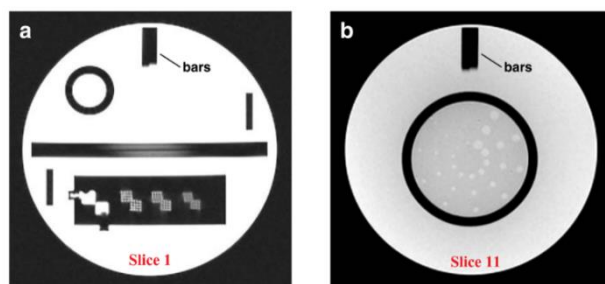


**Figure 36:** Images of slice 1 (a) and slice 11 (b) with the pairs of vertical bars from the 45° crossed wedges indicated.

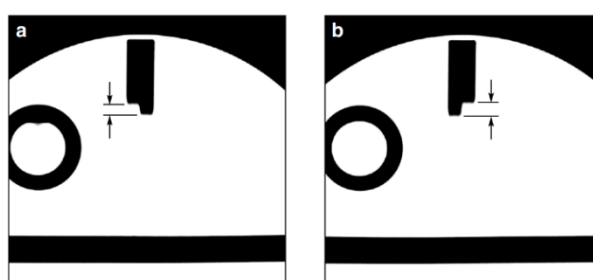


**Figure 37:** Images of slice 1 illustrating measurement of slice position error. The arrows indicate the bar length difference measurement that is to be made. (a) The bar on the right is longer, meaning the slice is mispositioned superiorly; this bar length difference is assigned a positive value (+). (b) The bar on the left is longer, meaning the slice is mispositioned inferiorly; this bar length difference is assigned a negative value (-).

**Table 28.** Slice position accuracy test result.

Series	Slice 1	Slice 11	Result
ACR T1	0	0.89	Pass
ACR T2 TE 20	0	-1.23	Pass
ACR T2 TE 80	0	-0.92	Pass
Clinical T1	-0.77	-0.78	Pass
Clinical T2	0	-1.38	Pass

**Recommended Action Criteria:** The magnitude of each bar length difference should be less or equal to 5 mm.

**Result:** PASSED



## 5. Image intensity uniformity

**Purpose:** To measure the uniformity of the image intensity over a large water-only region of the phantom lying near the middle of the imaged volume and thus near the middle of the head coil.

### Method

1. Display slice location 7.
2. Place a large, circular region-of-interest (ROI) on image. This ROI should have an area of between  $195 \text{ cm}^2$  and  $205 \text{ cm}^2$ .
3. Set the display window to its minimum and lower the level until the entire area inside the large ROI is white.
4. Measure low signal value by placing the small ROI roughly  $1 \text{ cm}^2$  at the region of dark pixels develops inside the large ROI.
5. Record the mean pixel value for this  $1 \text{ cm}^2$  ROI. This is the measured low-signal value.
6. Raise the level until all but a small, roughly  $1 \text{ cm}^2$  region of white pixels remains inside the large ROI. This is the region of highest signal.
7. Record the average pixel value for this  $1 \text{ cm}^2$  ROI. This is the measured high-signal value.

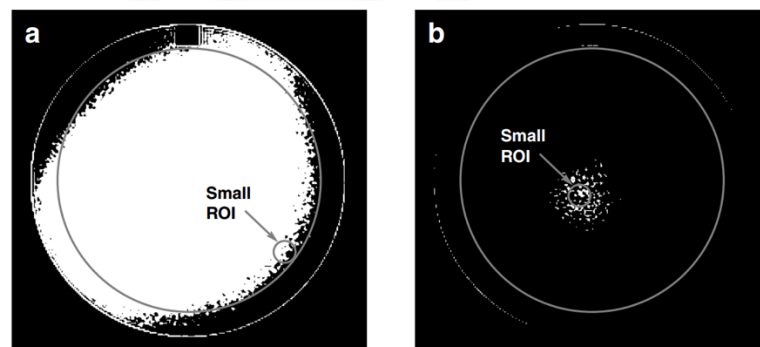


**Figure 38:** (right) ROI placement for low signal-value, (left) ROI placement for HIGH signal-value.

The measured high-and low-signal values for each of the ACR series are combined to produce a value called percent integral uniformity (PIU). Use the following formula to calculate PIU:

$$\text{PIU} = 100 \times \left(1 - \frac{(\text{high} - \text{low})}{(\text{high} + \text{low})}\right) \quad (\text{B.2})$$

**Table 29.** Image intensity uniformity test result.

Series	Low signal	High signal	PIU (%)	Result
ACR T1	1438.94	1443.49	99.84	Pass
ACR T2 TE 20	1513.24	1517.81	99.85	Pass
ACR T2 TE 80	827.93	835.43	99.55	Pass
Clinical T1	1554.95	1562.78	99.75	Pass
Clinical T1	958.03	972.00	99.28	Pass

**Recommended Action Criteria:** PIU should be greater than or equal to 87.5% for MRI systems with field strengths less than 3 Tesla.

**Result:** PASSED

## 6. Percent signal ghosting

**Purpose:** To assesses the level of ghosting in the image.

### Method

1. Display slice 7 of the ACR T1 series.
2. Using the workstation's ROI tool, 5 intensity measurements are made: Place a large ROI on the image an area between 195-205 cm<sup>2</sup>, and the average intensity in the background at 4 locations outside of the image area of the ROI about 10 cm<sup>2</sup>.
3. The value for the ghosting, as a fraction of the primary signal, is calculated using the following formula:

$$\text{Ghosting ratio} = \frac{(\text{top} + \text{btm}) - (\text{left} + \text{right})}{(2 \times \text{Large ROI})} \quad (\text{B.3})$$

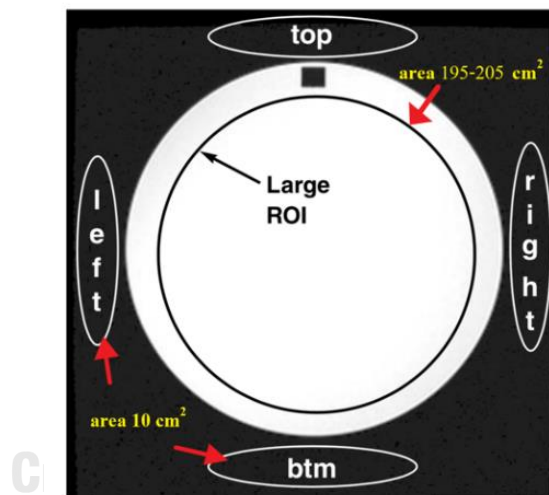


**Figure 39:** Image of slice 7 illustrating ROI placements for percent-signal ghosting measurements.

**Table 30.** Pixel value and result of percent signal ghosting test.

Series	Large	Top	Right	Left	Bottom	Calculated value	Result
ACR T1	1412.05	6.66	7.11	8.82	6.46	-0.0010	Pass
ACR T2 TE 20	1484.00	5.99	7.61	13.56	5.42	-0.0032	Pass
ACR T2 TE 80	808.16	5.53	6.26	5.91	4.07	-0.0016	Pass
Clinical T1	1522.06	7.81	5.25	10.47	7.53	-0.0001	Pass
Clinical T2	939.14	9.19	9.78	15.67	6.80	-0.0050	Pass

**Recommended Action Criteria:** The ghosting ratio should be less than or equal to 0.025.

**Result:** PASSED



## 7. Low contrast object Detectability

**Purpose:** To assesses the extent to which objects of low contrast are discernible in the images

### Method

The low-contrast objects appear on 4 slices: slices 8 through 11. In each slice the low-contrast objects appear as rows of small disks, with the rows radiating from the center of a circle like spokes in a wheel. Each spoke is made up of three disks, and there are ten spokes in each circle as show in figure 40. All the disks on a given slice have the same level of contrast. In order, from slice 8 to slice 11, the contrast values are 1.4%, 2.5%, 3.6%, and 5.1%. All the disks in a given spoke have the same diameter. Starting at the 12 o'clock position and moving clockwise, the disk diameter decreases progressively from 7.0 mm at the first spoke to 1.5 mm at the tenth spoke.

The measurements for this test consist of counting the number of complete spokes seen in each of the four slices. This is done for each of the 4 axial series.

Use the following procedure to score the number of complete spokes seen in a slice:

1. Display the slice to be scored. It helps to start with slice 11, which has the highest contrast objects.
2. Adjust the display window width and level settings for best visibility of the low-contrast objects.
3. Count the number of complete spokes and record the score.

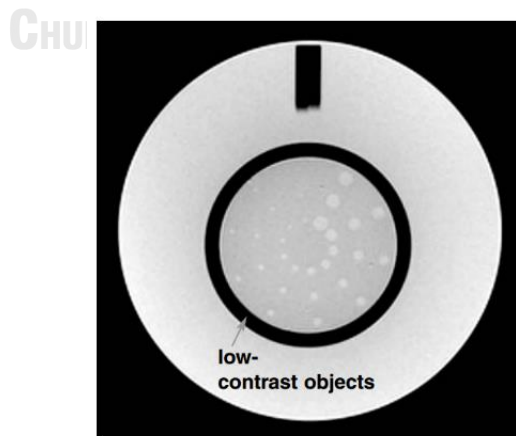


**Figure 40:** Image of slice 11 showing the circle of low contrast objects for the low-contrast object detectability test.

**Table 31.** The result of low contrast detectability test.

Series	Slice 8	Slice 9	Slice 10	Slice 11	Total	Result
ACR T1	7	8	9	10	34	Pass
ACR T2 TE 20	6	9	10	10	35	Pass
ACR T2 TE 80	4	7	9	10	30	Pass
Clinical T1	7	9	10	10	36	Pass
Clinical T2	2	7	8	10	27	Pass

**Recommended Action Criteria:** For both in the ACR series and clinical series should have a total score of at least 9 spokes.

**Result:** PASSED



## 8. Image Artifact Evaluation

**Table 32.** Image artifact evaluation.

Series	Excessive Ghosting		Excessive Truncation		RF Leak	Noise	DC offset	
	Pass	Fail	Pass	Fail	Pass	Fail	Pass	Fail
ACR T1	✓		✓		✓		✓	
ACR T2 TE 20	✓		✓		✓		✓	
ACR T2 TE 80	✓		✓		✓		✓	
Clinical T1	✓		✓		✓		✓	
Clinical T2	✓		✓		✓		✓	

**Table 33.** Image Artifact Evaluation

Series	Aliasing Artifact		Recon Artifact		Geometric Distortion	
	Pass	Fail	Pass	Fail	Pass	Fail
ACR T1	✓		✓		✓	
ACR T2 TE 20	✓		✓		✓	
ACR T2 TE 80	✓		✓		✓	
Clinical T1	✓		✓		✓	
Clinical T2	✓		✓		✓	

## 9. Magnet Visual Inspection

**Table 34.** Magnet Visual Inspection.

Visual Inspection	Pass	Fail
RF door flange is present and door lock works properly	✓	
Patient alarm works properly	✓	
Magnet bore lights are working properly	✓	
Patient fan is working properly	✓	
Positioning lights are working properly	✓	
Patient table works properly	✓	
RF coils stored properly, cables are insulated, no visual defects	✓	
Patient/operator intercom system works properly	✓	
Daily QA system implemented	✓	
Operator's monitor is calibrated properly (SMPTE)	✓	
Images on film match display images (SMPTE)	✓	



## Appendix C:

### Certificate of approval Institutional Review Board (IRB)



COE No. 018/2018

IRB No. 392/61

INSTITUTIONAL REVIEW BOARD

Faculty of Medicine, Chulalongkorn University

1873 Rama IV Road, Patumwan, Bangkok 10330, Thailand, Tel 662-256-4493

#### Certificate of Exemption

The Institutional Review Board of the Faculty of Medicine, Chulalongkorn University, Bangkok, Thailand, has exempted the following study in compliance with the International guidelines for human research protection as Declaration of Helsinki, The Belmont Report, CIOMS Guideline, International Conference on Harmonization in Good Clinical Practice (ICH-GCP) and 45CFR 46.101(b)

**Study Title** : Investigation of Parameters for Metallic Artifact Reduction using 3-D SPACE in MR Lumbar Spine at 1.5 Tesla: A Phantom Study

**Principal Investigator** : Miss Thanatchaya Lowong

**Study Center** : Department of Radiology, Faculty of Medicine, Chulalongkorn University.

Signature:

(Emeritus Professor Tada Sueblinwong MD)

Chairperson

The Institutional Review Board

Signature:

(Assistant Professor Prapapan Rajatapiti MD, PhD)

Member and Secretary

The Institutional Review

**Date of Exemption** : July 4, 2018

**Note** No continuing review report and final report when finish require

## VITA

<b>NAME</b>	Thanatchaya Lowong
<b>DATE OF BIRTH</b>	25 Oct 1991
<b>PLACE OF BIRTH</b>	Phayao, Thailand
<b>INSTITUTIONS ATTENDED</b>	Naresuan University, 2014: Bachelor of Science (Radiological Technology) B.Sc. (Radiological Technology)
<b>HOME ADDRESS</b>	69/304 Ratchapruek Road, Bangkhor, Chomthong, Thailand 10150
<b>PUBLICATION</b>	Lowong T., Prakkamakul S., Khamwan K. Investigation of Parameters for Metallic Artifact Reduction Using 3-D SPACE in MR Lumbar Spine: A Phantom Study. In Proceeding of 11th Annual Scientific Meeting of Thai Medical Physicist Society (TMPS), pp 120-121, Chonburi, Thailand, 2019
<b>AWARD RECEIVED</b>	International Scholarship from the 74th Japanese Society of Radiological Technology (JSRT), Japan